4-21-2023

The Luminous Power of Accretion Disks in Active Galactic Nuclei

Imogen Jade Courtney
Western Michigan University

The Luminous Power of Accretion Disks in Active Galactic Nuclei

Imogen Courtney

Lee Honors College Thesis

Abstract

Active Galactic Nuclei (AGN) are the most luminous long-lived objects in the universe. The phenomenon of the immense luminosities we observe for AGN has interested physicists and astronomers for over a century and continues to fascinate scientists today. The work in this thesis aims to provide an introductory exploration of this phenomenon. This thesis uses a simple model of AGN accretion disks that was developed under the standard disk model proposed by Shakura & Sunyev in 1973 under the simplest assumptions. The model accurately demonstrates how physical parameters, such as the temperature, radiative flux, luminosity, and spectra, scale through an AGN accretion disk. The model is applied for characteristic mass accretion rates and masses of the supermassive black holes (SMBH) found at the center of most AGN. The dependencies of the disk's luminous power on these parameters are identified. We find that the inner regions of an AGN accretion disk are the hottest and therefore emit the greatest share of the disk's luminosity. An accretion disk with a fixed mass accretion rate around a more massive SMBH is cooler than for a disk around a less massive one and is more luminous for greater accretion rates. The accretion disk spectra of AGN peak at ultraviolet (UV) wavelengths. For a fixed disk mass accretion rate, the accretion disks around less massive black holes are hotter and therefore have spectra that peak at shorter UV wavelengths and vice versa for spectra of accretion disks around more massive black holes. The shorter wavelengths in the observed spectrum are largely confined to arise and peak within inner regions of the disk where the temperature is hotter, whereas longer wavelengths are emitted from a broader range in the disk and peak in the outer disk where the temperature is cooler. We also applied a perturbation to the disk temperature through the inner section of the disk from the innermost circular stable orbit to $r = 400\ R_g$ to simulate with a simple model the highly variable nature of AGN. This model saw the shortest wavelengths contributing to the total luminosity of an accretion disk changed in their emission the most, as these wavelengths arise most prominently from the inner disk where our disk's temperature was perturbed, and the wavelengths which have significant contributions to the spectrum outside of $r = 400\ R_g$ fluctuated less.

1. Introduction

1.1. Introductory Concepts

Active Galactic Nuclei (AGN) are the most luminous long-lived objects in the universe. Galaxies are hosts to millions of stars and other matter comprised of gas and dust. The galaxy's nucleus (or AGN) is the central compact region about which the galaxy's stars, gas, and dust orbit. The question of where their immense power comes from has fascinated physicists and astronomers for over a century. Below is a brief history of the discovery of AGN and their cosmic context. A description of how an accretion disk is formed is also provided.

History and Cosmic Context of AGN

The discovery of AGN began in the early 1900s when Edward Fath made the first observations of emission lines from galactic nuclei in 1908 (Shields, 1999). Many others contributed to additional observations over the following decades, advancing the knowledge of emissions from various AGNs. In 1943 Carl Seyfert published a study of six galaxies where he named classification categories for AGN dependent on their spectra. There are many classification categories of AGN, which developed over years of discovery.

One category, quasars, was discovered in the 1960s following a surge of advances in radio astronomy in the 1950s (Shields, 1999). Quasars are the most luminous AGNs, with luminosities ranging from 10^{38} W to 10^{41} W (Carrol & Ostlie, 2018). The typical value of the luminosity of a quasar is 10^{39} W. This project focuses on AGN that fall into the quasar category, with luminosities ranging between 10^{36} W and 10^{41} W. These immense luminosities observed from quasars remain the most luminous objects observed in the universe since their discovery in the 1960s. The unknown source of the power of AGN has sparked many years of dedication to unveil a complete understanding of AGN. This pursuit continues today.

Figures 1.1(a) and 1.1(b) show images of two AGN that have been observed. Figure 1.1(a) is an image of the quasar 3C 273 where the luminosity is so great that the galaxy surrounding the AGN cannot be seen on this scale. In comparison, Figure 1.1(a) is an image of the AGN NGC 5548, where the luminous power of the AGN scales roughly one-to-one with the total luminous power of the galaxy.

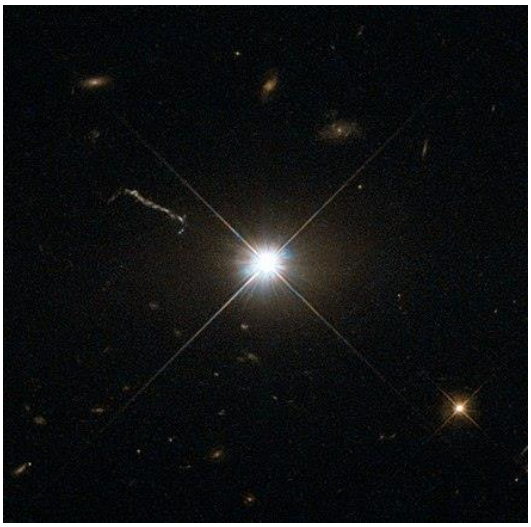

Figure 1.1(a) – An image taken by the Hubble Telescope of the quasar 3C273. Image Credit: (Hille, 2013)

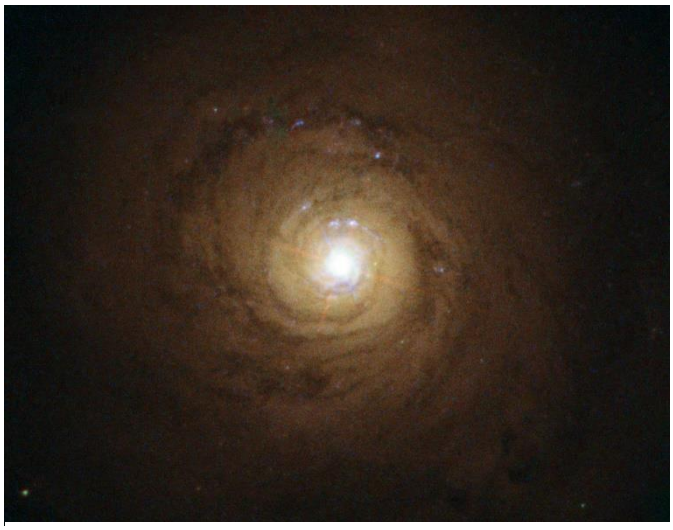

Figure 1.1(b) – An image taken by the Hubble Telescope of the AGN NGC 5548. Image Credit: (*Supermassive black hole at the heart of NGC 5548*. (n.d.).)

Through observations and the dedication to understanding these complex objects, it has been established that a supermassive black hole (SMBH) is known to lie at the center of all AGN. A black hole is an immensely dense region of space whose gravitational field is so strong that nothing, including light, can escape its field. A SMBH is a black hole whose mass ranges from a million to a billion times the mass of the sun (Carroll & Ostile, 2018), 10^6 $M_\odot$ to 10^9 $M_\odot$ - where $M_\odot$ is the standard symbolic notation for the mass of the sun whose value can be found in Table 7.1.

Since nothing can escape a black hole, or SMBH, they cannot be observed directly but by their influence on surrounding matter. It is generally agreed that AGNs' luminous power and energy are produced from matter accreting onto the SMBH, where some fraction of the mass accreted is converted into luminous energy and powerful jets of relativistic ions. Figure 1.2 shows an artist rendition of what physicists think the structure of an AGN might look like; a SMBH located at the center with an accretion disk immediately surrounding the SMBH, and a surrounding collection of gas and dust from the host galaxy which feeds the accretion disk. Figure 1.3 shows the relativistic jet emitted from the AGN of galaxy M87.

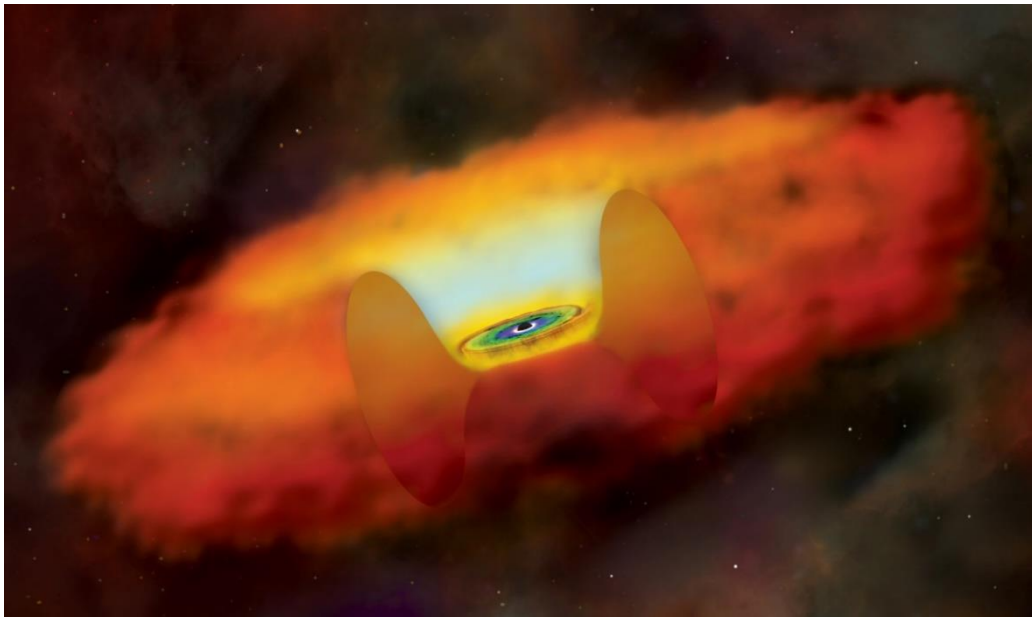

Figure 1.2 – An artist's rendition of the structure of an AGN. Image Credit: (*Chandra: Resources: Quasars & agns(Illustrations)*. (n.d.).)

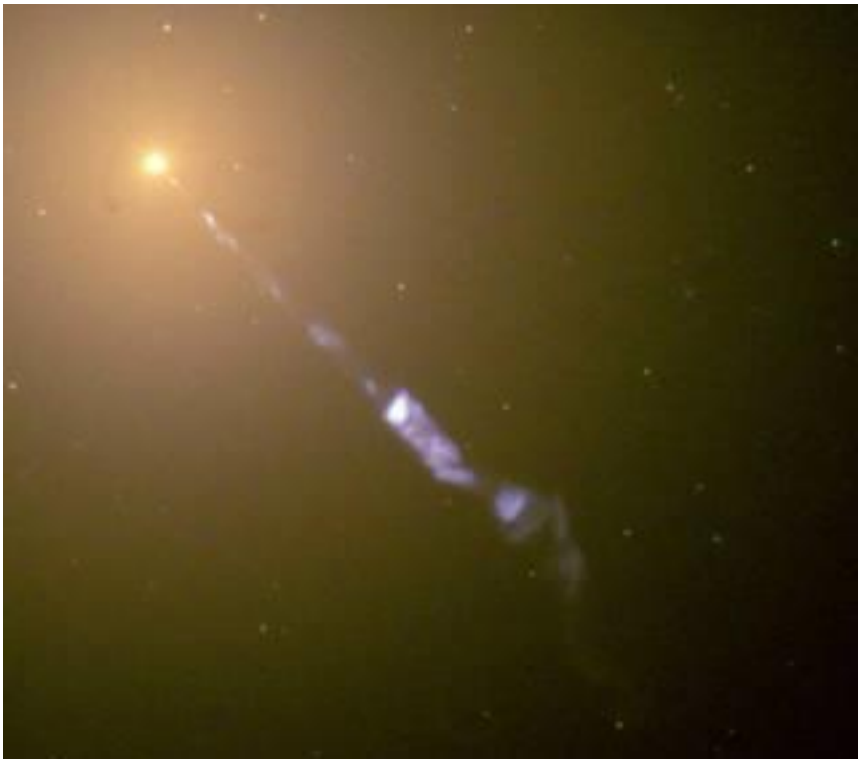

Figure 1.3 – An image taken by the Hubble Telescope of the relativistic jet emitted by the AGN of M87, a galaxy located 54 million light years from the Earth (Garner, 2017). Image Credit: (Garner, 2017)

One key characteristic of AGN is that they are highly variable, and the cause of their variability is not precisely known. There have, however, been many attempts to theorize the mechanisms causing variability; however, they remain only theories. Another aspect of AGN that is not well defined is the rotational dependency of the SMBH within AGN. It is known that SMBHs within AGN rotate, but the importance of the case of the rotating black hole is not fully understood. That is why only the case for the non-rotating black hole will be considered in this project. To ensure the details outlined in this paper apply as generally as possible, the parameter setting the rotation of the black hole has been left in the derivations of equations.

Understanding accretion disks and the AGN phenomenon contributes to the general exploration and understanding of the evolution of galaxies and the universe. This project uses the Shakura & Sunayev standard accretion disk model (1973) under the simplest assumptions. The results from this model will be used to describe several characteristics of accretion disks, including their temperature, radiative flux, luminosity (total power), and the emitted spectrum. We will model four different accretion disks, with varying masses of the SMBH central to the AGN accretion disk and varying mass accretion rates (more discussion will follow on these parameters).

Formation of an Accretion Disk

To understand how an accretion disk is formed, we first consider the simplest case: a black hole semidetached binary system. The solution to this system follows the solution to the Keplerian two-body orbit problem. In this case, mass transfers from the secondary star to the primary star (usually a black hole) through the inner Lagrangian point when the secondary star has filled its Roche lobe (Carroll & Ostlie, 2018). The Roche lobe is a figure of eight outline (Figure 1.4) that defines the points in space with equal effective gravitational potential energy per unit mass. The inner Lagrangian point is the crossover point between the primary and secondary stars in the figure-of-eight outline. It is a point of equilibrium between the gravitational forces experienced by the two stars. As matter from the star falls in through the inner Lagrangian point, the orbital motion of the binary system and the angular momentum of the mass accreting prevent the transferred mass from falling directly into the black hole. Instead, it

falls into an accretion disk that orbits around the black hole while conserving angular momentum.

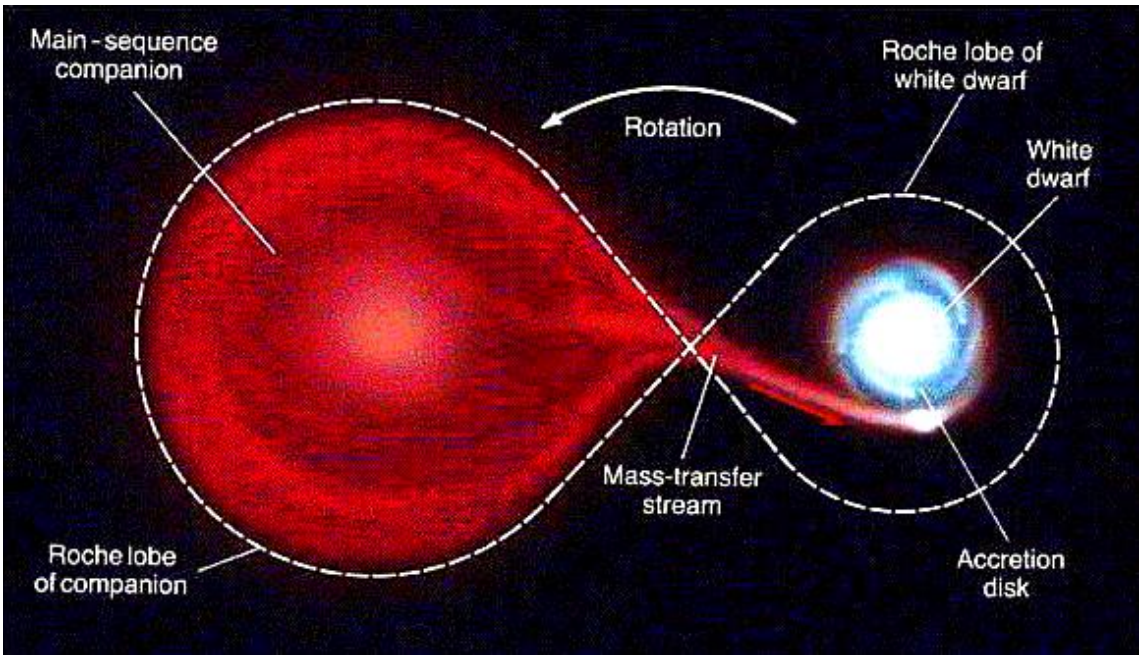

Figure 1.4 – An image showing the figure of eight Roche Lobe outline which the secondary star (Main-sequency companion) transfers mass through the crossover point of the figure of eight, the inner Lagrangian point forming an accretion disk. This image uses a white dwarf as the compact object of the primary star, but in the case of black hole binary systems, the white dwarf would be replaced with a stellar mass black hole. Image Credit: ("Chandra: Educational materials", n.d.)

Cygnus X-1 is an example of a stellar-mass black hole (21 $M_{\odot}$) in a semidetached binary system. It is located in our galaxy, the Milky Way, about 6,000 light-years from Earth. (A light year is a constant value of the distance that light can travel in one year, and its value can be found in Table 7.1). Figure 1.5 shows an artist's rendition of the semidetached binary system that hosts Cygnus X-1, which shows mass falling through the inner Lagrangian point from the secondary star, forming an accretion disk. The image also shows relativistic jets emitted from Cygnus X-1, which were previously discussed in this section.

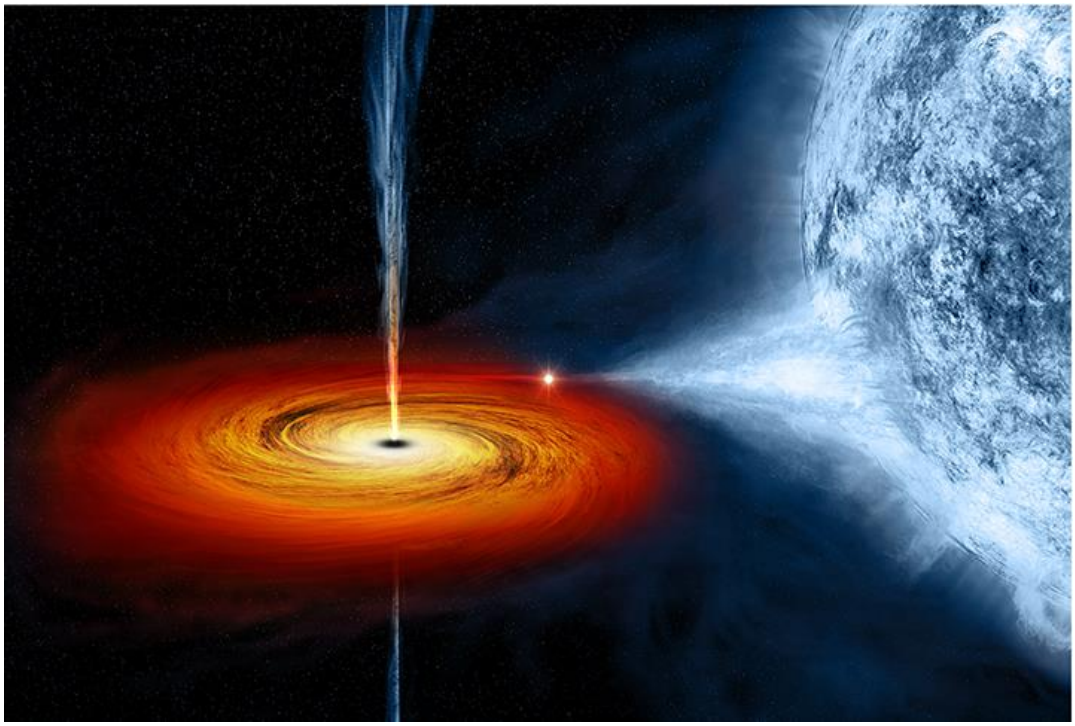

Figure 1.5 – An artist rendition of the black hole binary system which hosts the stellar mass black hole Cygnus X-1. The image shows the secondary star transporting mass to the accretion disk around the black hole. Image Credit: (Anderson & Watzke, 2011)

For the case of AGN, the process is somewhat different because there is no singular source powering the formation of an accretion disk. Nevertheless, gaseous matter from the host galaxy finds its way into an accretion disk by falling into the immense gravitational potential well of the SMBH. Like the semidetached binary system, the angular momentum of the mass accreting into the accretion disk prevents the matter from falling directly into the SMBH. What happens once the matter is brought into the accretion disk will be discussed further in Section 2.1.

1.2. Organization of the paper

Here, we briefly outline the organization of the paper. Section 2 details the structure of an accretion disk, which includes a detailed discussion of the equations used to build the models. This section focuses on an accretion disk's temperature, radiated flux, and luminosity.

Section 3 details the spectrum of an accretion disk, including a brief exploration of the additional equations and principles required to build the model for the disk spectrum. We look at the contributions of different wavelengths throughout the disk and the total luminosity spectrum produced for accretion disks.

Section 4 discusses the variability of the luminosity of AGN accretion disks and outlines a simple model to represent their variability. The contributions of specific wavelengths to the spectrum and the spectrum itself are compared to an unvaried disk, and the impacts on the spectrum of the simple variability model are analyzed.

The final Section of this paper will outline the conclusions from each section.

2. Accretion Disk Structure

2.1 Physical Considerations

The model devised in the following sections was developed under the Shakura & Sunyaev standard accretion disk model (1973). This is a simple model of a geometrically thin, optically thick accretion disk, where the structure is dictated by choices in the mass of the SMBH, M, the disk mass-accretion rate (the time derivative of mass accretion), M_{dot}, and the ratio, x, of the innermost stable circular orbit (ISCO), R_{in}, to the gravitational radius (defined in Eq. (2.28)), R_g ($x = R_{in}/R_g$).

Assumptions

The simplest assumptions for a simple accretion disk model were used. First, we assume that the accretion disk is azimuthally symmetric and approximately cylindrical (Pereyra et al., 2006). The thickness of the disk is not constant and varies with radial distance; however, under our assumption of a thin accretion disk, we assume that the height of the disk h, measured from the midplane through the disk, is much less than the radius r at every point in the disk ($h << r$).

Optical depth measures the number of times light (across all wavelengths) can travel the average distance between collisions before reaching the disk's surface (Carroll & Ostlie, 2018). Under our assumption that the accretion disk is optically thick, we assume that over all the wavelengths emitted from the disk, the optical depth τ, as measured from the midplane of the disk at radius r, is:

$$\tau = \int \kappa\rho \, dz \gg 1, \tag{2.1}$$

where z is measured vertically upward from the midplane in the disk, κ is the radiative opacity at radius r, and ρ is the mass density at radius r. Under these conditions, the total height of the disk is approximately 2h, and the optical depth is approximately 2τ. Figure 2.1 shows the shape of an accretion disk under our assumptions.

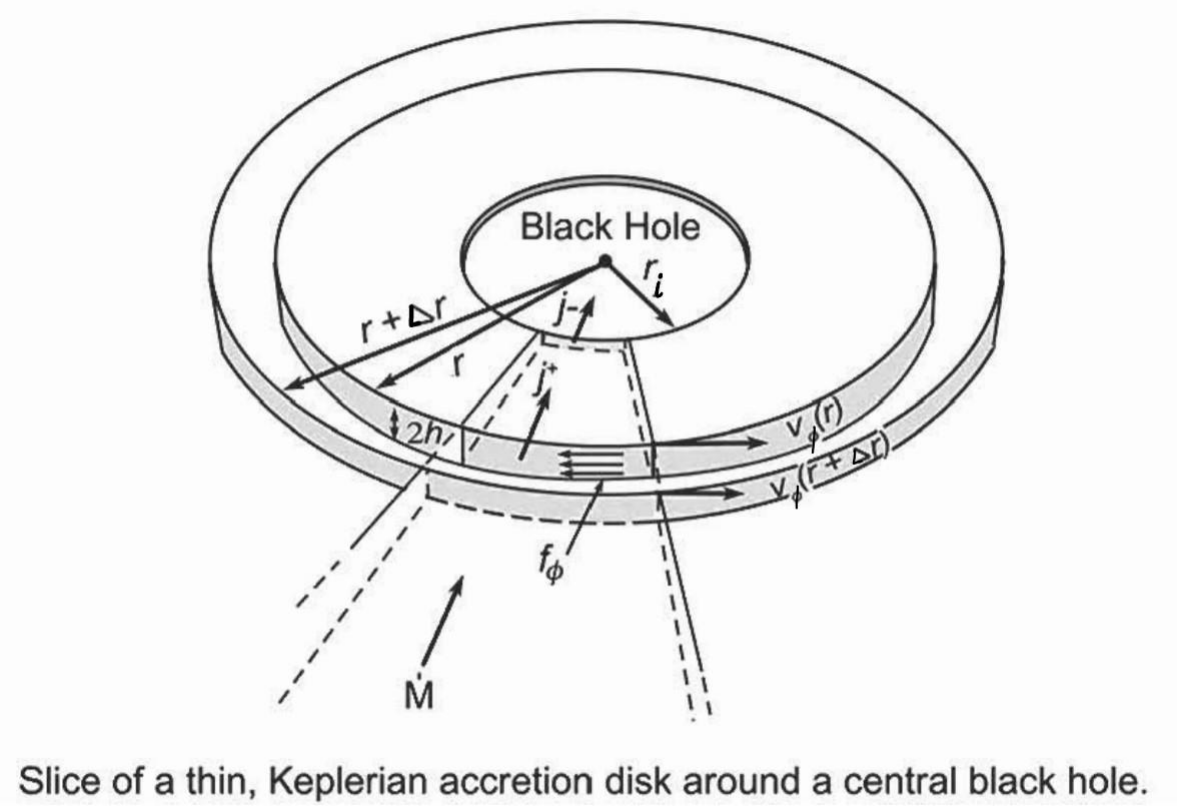

Figure 2.1 – An image showing the structure of an accretion disk, which can be seen to be azimuthally symmetric and cylindrical in shape, with a total height of 2h. Other parameters seen in the figure include: 1) the inner most circular stable orbit r_i, 2) the distance between two adjacent radial points Δr such that r and r + Δr are adjacent, 3) the orbital speed at the two radial points $v_\phi(r)$ and $v_\phi(r + \Delta r)$, 4) the quasi-static flow of mass per unit time $\dot{M}$, 5) the inward rate of angular momentum transport j+ at radius r, and 6) the consumption rate of angular momentum j- by the SMBH at r_i. Image Credit: ("Steady State Accretion Disk Model", n.d.) – with corrections by-hand to notational errors.

Next, we assume that the gravitational field of the accretion disk is Newtonian (Pereyra et al., 2006). This is a fair approximation if the model remains well outside the event horizon of the SMBH. The event horizon is the boundary at which nothing can escape the immense gravitational pull of the black hole. Non-rotating black holes are governed by the Schwarzschild Metric, which defines the event horizon to be (Carroll & Ostlie, 2018):

$$R_s = \frac{2GM}{c^2}, \tag{2.2}$$

where G is the gravitational constant, c is the speed of light, M is the mass of the SMBH, and R_s is the radius of the event horizon, also known as the Schwarzschild radius. For the duration of this model, we consider a non-rotating SMBH with an ISCO of $3R_s$. For a SMBH of mass 10^8 $M_\odot$, this ISCO is approximately 6 AU, where 1 AU (Astronomical Unit) is the average distance from the Sun to the Earth. Thus, the assumption of the gravitational field governing the accretion disk being Newtonian is valid.

The mass of the accretion disk must be negligible compared to the SMBH's, such that the matter accreting onto the SMBH only experiences the gravitational pull from the black hole (Pereyra et al., 2006). If this is the case, the path of matter accreting onto the SMBH is assumed to follow circular Keplerian orbits. This assumption is only approximately true. That is, if the matter were truly following a Keplerian orbit, it would not be accreting but remaining at a fixed radius.

The accretion disk is also considered steady, with a constant amount of mass entering and leaving the disk and no mass build up (Pereyra et al., 2006). We assume the outermost stable orbit, R_{out} is much greater than the ISCO R_{in}, and shear stress is responsible for transporting mass from R_{out} to R_{in}. Shear stress is a friction force that acts between the layers of accreting matter, shown by arrows in Figure 2.1 labeled as f_ϕ. Shakura and Sunyaev (1973), who referred to the shear stress as viscosity, suggested that the shear stress f_ϕ was directly proportional to the local gas pressure P_{gas} since the frictional force acts against the flow of the gas at radius r. This relationship is, therefore:

$$f_\phi = \alpha P_{gas}, \tag{2.3}$$

where α is a dimensionless constant, and shear stress has units of N m^{-2}, (Newton per square meter). This shear stress creates a torque W at each radius r, given by ("Steady State Accretion Disk Model", n.d.):

$$\mathrm{W} = 2\pi r^2 H f_\phi, \tag{2.4}$$

where H is the full height of the disk, and torque has units of N m, (Newton meter). The torque W is responsible for removing the angular momentum or mass at each radius, allowing the mass

to accrete into the inner regions of the disk. We assume that conservation of angular momentum holds as shear stresses cause the matter in the disk to accrete and that R_{in} is the last stable orbit of the accretion disk, and at this radius, the shear stress is equal to zero.

The final two assumptions we invoke are that conservation of energy holds as matter accretes and loses gravitational potential energy, which is converted into radiation (Pereyra et al., 2006). Finally, we assume that the local surface emission of the accretion disk is blackbody.

Blackbody Radiation

As previously mentioned, we assume that the local surface emission is blackbody. Blackbody radiation is emitted from an 'ideal emitter,' also known as a blackbody (Carroll & Ostlie, 2018). A blackbody has a temperature above absolute zero (0 K) and emits and absorbs light across all wavelengths at maximum efficiency. An ideal emitter with maximum efficiency must absorb all incident light and radiate all the energy absorbed as a characteristic spectrum.

Stars and planets are approximated to be blackbodies; however, they are not ideal blackbodies. This means we find their effective temperature, the temperature of an ideal blackbody emitting the same amount of electromagnetic radiation. The characteristic spectrum of a blackbody at temperature T is a function of wavelength as given by (Carroll & Ostlie, 2018):

$$B_\lambda(T) = \left(\frac{2hc^2}{\lambda^5}\right)\left(\frac{1}{e^{\frac{hc}{\lambda kT}} - 1}\right), \tag{2.5}$$

where $B_\lambda(T)$ is known as Planck's function, h is Planck's constant, and k is the Boltzmann constant. The values of both constants can be found in Table 7.1. This function of specific intensity has units of W m^{-2} nm^{-1} sr^{-1}, (Watts per square meter per nanometer per steradian), where a nanometer, nm = 10^{-9} m, is the unit of the wavelength of light.

From Planck's function at wavelength λ, the radiative energy flux of a blackbody source can be found. Radiative energy flux is the net flow of surface emission per unit area, which we find by integrating over the solid angle which is given as:

$$d\Omega = \sin\theta \, d\theta d\varphi, \tag{2.6}$$

where θ is the angle measured from the normal of the emitting surface, and φ is the horizontal angle. We assume that each patch of surface area, dA emits blackbody radiation equally in all directions onto an outward hemisphere and we assume there is no radiation incident on the surface, which allows us to consider only the outward radiation. The disks specific surface flux F_λ, in units of W m^{-2} nm^{-2}, over 2π steradians of the solid angle for the outward hemisphere is (Carroll & Ostlie, 2018):

$$F_\lambda = \int_0^{2\pi} \int_0^{\frac{\pi}{2}} B_\lambda(T) \cos\theta \sin\theta \, d\theta \, d\varphi = \pi B_\lambda(T). \tag{2.7}$$

The total flux emitted across all wavelengths F, in units of W m^{-2}, is then found:

$$F = \int_0^{\infty} F_\lambda \, d\lambda. \tag{2.8}$$

Using Eq. (2.5) and performing the integrations, the total outward surface flux emitted by a blackbody is:

$$F = \frac{2\pi^5 k^4}{15c^2h^3} T^4 = \sigma_{SB} T^4, \tag{2.9}$$

where σ_{SB} is the Stefan-Boltzmann constant, a combination of the constants shown in Eq. (2.9) whose value can be found in Table 7.1.

The radiation emitted from a blackbody of effective temperature T is a continuous spectrum with energy contributions at all wavelengths. Figure 2.2 is a graph of $B_\lambda(T)$ vs. λ for three characteristic effective temperatures found in AGN accretion disks modeled in this paper.

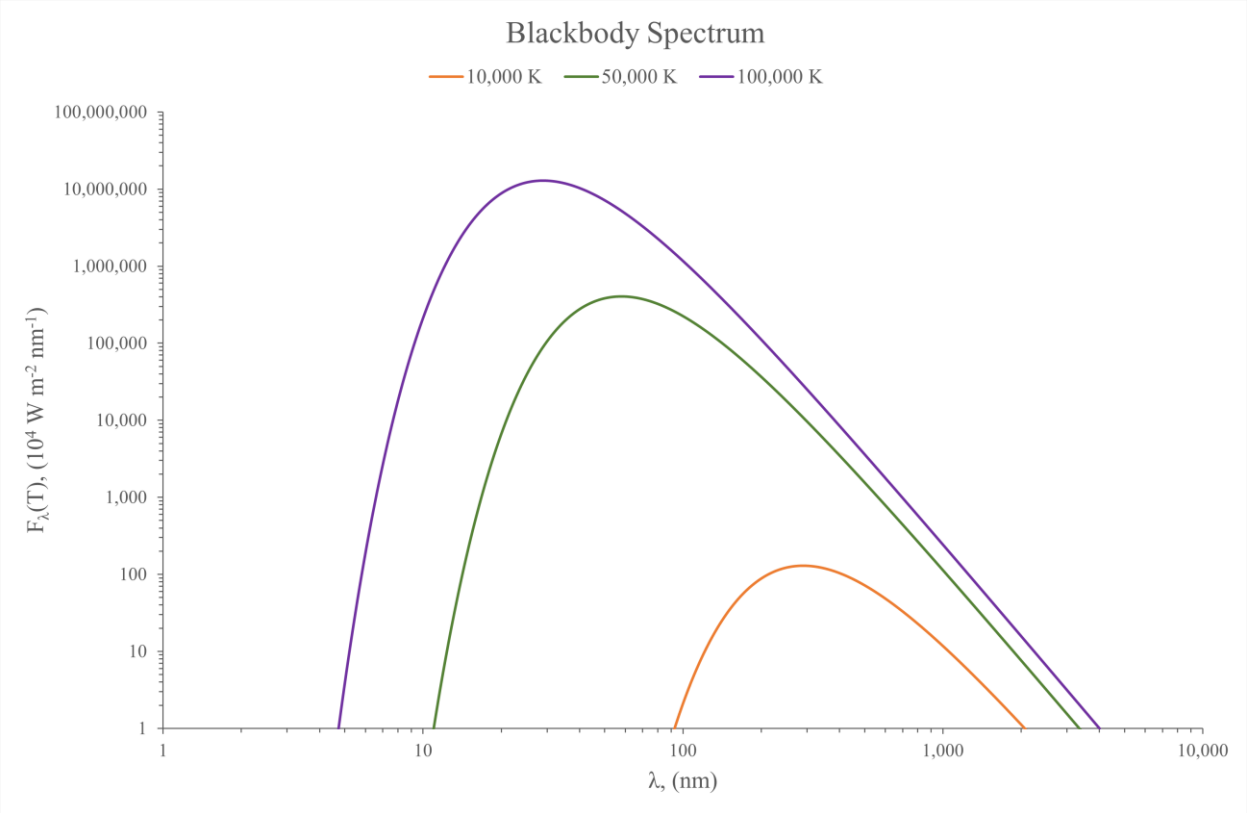

Figure 2.2 – A graph of the specific radiative flux vs. wavelength for three different effective blackbody temperatures that are representative of temperatures we find throughout AGN Accretion Disks.

Figure 2.2 demonstrates how a hotter blackbody emits a greater radiative flux than a cooler blackbody as shown by the difference in the area under each of the three curves. The shape of the curves, a result of Plank's function, shows that not all wavelengths contribute equally to the total radiative flux emitted from a blackbody. In fact, the peak of the blackbody function moves to shorter wavelengths for a hotter emitter. The relationship between the effective temperature of a blackbody and the wavelength at which that blackbody function peaks at is given by Wien's Law, which is found by taking the derivative of the function $B_\lambda(T)$ with respect to λ at a constant temperature and setting it equal to zero:

$$\left.\frac{\partial B_\lambda}{\partial \lambda}\right|_T = 0. \qquad (2.10)$$

This gives:

$$\frac{hc}{\lambda_{max}} = 4.96511kT, \tag{2.11}$$

where λ_{max} is the wavelength at which the blackbody spectrum peaks. Substituting the values of the constants into and rearranging Eq. (2.11) gives:

$$\lambda_{max} = \frac{2.897771955 \times 10^6}{T}\ nm, \tag{2.12}$$

where T is in units of Kelvin (K). These equations, (2.11) and (2.12), are known as Wien's Law. Wien's Law shows that as the temperature of the blackbody increases, λ_{max} becomes shorter. The Stefan-Boltzmann Law, given by Eq. (2.9), shows that over all wavelengths, a hotter blackbody emits more energy per second per unit area. This can be seen in Figure 2.2, where the blackbody with the higher effective temperature peaks at a shorter wavelength and higher intensity.

Mechanical Energy of the Disk

We consider an accretion disk around a SMBH to be a bound system in equilibrium and therefore governed by the virial theorem. The virial theorem equates the time-averaged, total kinetic, and gravitational potential energy of the system and is given by (Carroll & Ostlie, 2018):

$$2K + \Omega_{gr} = 0, \tag{2.13}$$

where K is the kinetic energy, and Ω_{gr} is the gravitational potential energy. From this theorem, the average kinetic energy of the system is given by:

$$K = -\frac{1}{2}\Omega_{gr}. \tag{2.14}$$

We assume the gravitational field which hosts the accretion disk to be Newtonian (Pereyra et al., 2006). Therefore, the average gravitational potential energy of the system for a mass m, located in a gravitational field created by a SMBH of mass M, at a distance r from the SMBH is given by:

$$\Omega_{gr} = -\frac{GMm}{r}. \tag{2.15}$$

The total mechanical energy of the accretion disk E is the sum of the average kinetic and gravitational potential energy of the system and is therefore given by:

$$E = K + \Omega_{gr} = \frac{1}{2}\Omega_{gr} = -\frac{GMm}{2r}. \tag{2.16}$$

Another assumption we make is that the mass of the disk remains constant. That is that the disk is a steady-state mass-accretion disk (Pereyra et al., 2006). Given this assumption, the rate at which mass m enters and leaves the accretion disk is given by:

$$m = M_{dot}\Delta t, \tag{2.17}$$

where Δt is the time integral over which the total gravitational potential energy of the system changes, and M_{dot} is the mass-accretion rate in the disk. Substituting this into Eq. (2.17) reveals that the total mechanical energy of the disk is given by:

$$E = -\frac{GMM_{dot}\Delta t}{2r}. \tag{2.18}$$

The Temperature of the Disk

To find the temperature of the accretion disk, we invoke the assumption that conservation of energy holds as the loss in the gravitational potential energy of the mass within the disk is converted to radiation (Pereyra et al., 2006).

$$dE_{rad} = \frac{dE}{dr}dr = \frac{d}{dr}\left(-\frac{GMM_{dot}\Delta t}{2r}\right)dr = \frac{GMM_{dot}\Delta t}{2r^2}dr, \tag{2.19}$$

where dE_{rad} is the energy radiated away from the disk at radius r over the time interval Δt. Through dimensional analysis, the luminosity of the disk, defined as the amount of electromagnetic radiation radiated away from the disk per unit time (the rate of change of radiative flux), at radius r (dL_{ring}), is then:

$$dL_{ring}(r) = \frac{dE_{rad}}{\Delta t} = \frac{GMM_{dot}}{2r^2}dr. \tag{2.20}$$

To relate the luminosity of the disk, as written above, to the disk's temperature, we assume that at radius r, the disk's surface emission is locally blackbody. The total surface flux

emitted from a blackbody, the Stefan-Boltzmann Law, was previously outlined and given by Eq. (2.9). This law also gives the luminosity of the disk at radius r, under the assumption stated to be:

$$L_{ring}(r) = A_{ring}(r)\sigma_{SB}T_{eff}(r)^4, \tag{2.21}$$

where $T_{eff}(r)$ is the effective temperature of the disk at radius r, and $A_{ring}(r)$ is the surface area of the two-sided accretion disk at radius r, which is:

$$dA_{ring}(r) = 2 \times 2\pi r dr. \tag{2.22}$$

Combining the Stefan-Boltzmann equation, given by Eq. (2.21), and the derived surface area of the two-sided accretion disk, the luminosity of the disk at radius r, is then:

$$dL_{ring}(r) = 4\pi r\sigma_{SB}T_{eff}(r)^4 dr. \tag{2.23}$$

Equating this equation, Eq. (2.23), to the equation for the luminosity of the disk at radius r derived from the conservation of energy, Eq. (2.20), the effective temperature of the disk can be expressed as:

$$T_{eff}(r) = \left(\frac{GMM_{dot}}{8\pi\sigma_{SB}r^3}\right)^{\frac{1}{4}}. \tag{2.24}$$

The ISCO, R_{in}, is a crucial parameter of accretion disks. The effective temperature of an accretion disk can be expressed in terms of R_{in} and is then:

$$T_{eff}(r) = \left(\frac{GMM_{dot}}{8\pi\sigma_{SB}{R_{in}}^3}\right)^{\frac{1}{4}}\left(\frac{R_{in}}{r}\right)^{\frac{3}{4}}. \tag{2.25}$$

A better estimate given by Shakura and Sunyaev (1973) in their outline of the standard disk model gives Eq. (2.25) to be:

$$T_{eff}(r) = \left(\frac{3GMM_{dot}}{8\pi\sigma_{SB}{R_{in}}^3}\right)^{\frac{1}{4}}\left(\frac{R_{in}}{r}\right)^{\frac{3}{4}}\left(1 - \sqrt{\frac{R_{in}}{r}}\right)^{\frac{1}{4}}. \tag{2.26}$$

It is important to note the two changes seen in Eq. (2.26) from Eq. (2.25). The first change is the addition of the final parenthesis, which is a result of the inner boundary condition where there is no torque present at the ISCO. This factor provides a mathematical solution to

account for the decrease in dissipation from the maximum to the ISCO where no dissipation occurs. Without this factor, the temperature would continue to grow until reaching the ISCO when it would suddenly drop to zero because there is no torque, and therefore no dissipation. To avoid this discontinuity, this factor is imposed to provide a more physical representation of how the temperature changes as we approach the ISCO of the disk.

The second change is the appearance of the factor of three in the first parenthesis. This arises due to the transfer of angular momentum (Zdziarski et al., 2022). The factor of one in this parenthesis in Eq. (2.25) is a result of only considering the locally released gravitational potential energy, however, as previously noted that the transfer or angular momentum is responsible for the formation of an accretion disk, it is important to consider this factor in this model.

Additionally, the first parenthesis of Eq. (2.26) contains only physical constants and parameters that remain constant for a particular disk. Therefore, this factor sets a scale for the temperature of the accretion disk, however, is commonly defined and known as the characteristic disk temperature (T_{disk}). T_{disk} is then:

$$T_{disk} = \left(\frac{3GMM_{dot}}{8\pi\sigma_{SB}{R_{in}}^3}\right)^{\frac{1}{4}}. \tag{2.27}$$

The standard definition of T_{disk} as 'the characteristic disk temperature' can be misleading and is better defined as the temperature scale of the accretion disk. This defines the role T_{disk} plays in determining the temperature of an accretion disk at a particular radial point better because every temperature of the disk (at different radial points) scales directly from this number.

At the beginning of this section, it was mentioned that one of the key input parameters for a standard model accretion disk is the ratio between the ISCO, R_{in}, and the gravitational radius, R_g. The ISCO is therefore defined by these two parameters, as stated below:

$$R_{in} = xR_g, \tag{2.28}$$

where x is the ratio between R_{in} and R_g, which for non-rotating black holes, has a fixed value of x = 6. The gravitational radius, R_g, is defined to be:

$$R_g = \frac{GM}{c^2} = 1.4766 \times 10^{11}\left(\frac{M}{M_8}\right)(meters), \tag{2.29}$$

where $M_8 = 10^8\ M_\odot$ which is a characteristic mass of a SMBH found in an AGN. For a non-rotating black hole, the ISCO orbit is therefore only dependent on the mass of the black hole; however, the parameter x will continue to be discussed so that the model can be applied more generally. By substituting Eq. (2.28) and Eq. (2.29) into Eq. (2.27), the characteristic temperature of the disk is then:

$$T_{disk} = \left(\frac{3M_{dot}}{8\pi\sigma_{SB}G^2M^2x^3}\right)^{\frac{1}{4}}. \tag{2.30}$$

The temperature of the disk has been shown to vary throughout the disk. Therefore, a maximum temperature occurs at some annulus at a point r/R_{in}. To find the maximum temperature and the position through the disk where the maximum temperature occurs, we invoke a new parameter U which we define to be:

$$U = \frac{R_{in}}{r}. \tag{2.31}$$

Substituting this parameter into Eq. (2.26) gives it to be:

$$T_{eff}(U) = T_{disk}(U)^{\frac{3}{4}}\left(1-\sqrt{U}\right)^{\frac{1}{4}}. \tag{2.32}$$

We are now able to find the maximum temperature by taking the first derivative and setting it equal to zero:

$$\frac{dT_{eff}(U)}{dU} = 0 = 3U^{-\frac{1}{4}}\left(1-\sqrt{U}\right)^{\frac{1}{4}} - U^{\frac{3}{4}}\left(1-\sqrt{U}\right)^{-\frac{3}{4}}\left(\frac{1}{2\sqrt{U}}\right). \tag{2.33}$$

Rearranging Eq. (2.33), the value of U is found to be:

$$U = \frac{R_{in}}{r} = \frac{36}{49}. \tag{2.34}$$

This equation is rearranged to give the point through the disk where the maximum temperature occurs and is found to be at $r \approx 8.16R_g$. Substituting the value given in Eq. (2.34) into Eq. (2.32) and solving, the maximum temperature of the disk (T_{max}) is found to be:

$$T_{max} = T_{disk}\left(\frac{36}{49}\right)^{\frac{3}{4}}\left(1-\sqrt{\frac{36}{49}}\right)^{\frac{1}{4}} = 0.48787T_{disk}. \quad (2.35)$$

Therefore, the maximum temperature of the disk is approximately half of the characteristic temperature of the disk, T_{disk}. It is therefore important to note that there is no point through the disk where the temperature equals T_{disk}, reinforcing our discussion that T_{disk} sets the scale of the run of effective temperature with radius through the accretion disk.

The Luminosity of the Disk

The luminosity of the disk is derived by integrating the Stefan-Boltzmann Equation, Eq. (2.23), from the ISCO to the outer radius, ($r = R_{in}$ to $r = R_{out}$). The result of this integration is shown below:

$$L_{disk} = \int_{R_{in}}^{R_{out}} 4\pi r\sigma_{SB}T_{eff}(r)^4\, dr = \frac{4}{3}\pi\sigma_{SB}{R_{in}}^2{T_{disk}}^4\left[1-3\left(\frac{R_{in}}{R_{out}}\right)-2\left(\frac{R_{in}}{R_{out}}\right)^{\frac{3}{2}}\right]. \quad (2.36)$$

In the case of the infinite disk, or when the outer radius is much greater than the ISCO, $\frac{R_{in}}{R_{out}}$ becomes negligible, and so Eq. (2.36) becomes:

$$L_{disk} \approx L_{disk\,\infty} = \frac{4}{3}\pi{R_{in}}^2\sigma_{SB}{T_{disk}}^4. \quad (2.37)$$

Substituting in the equation for T_{disk}, given by Eq. (2.27), for the fully integrated luminosity of a finite disk is then:

$$L_{disk} = \frac{GMM_{dot}}{2R_{in}}\left[1-3\left(\frac{R_{in}}{R_{out}}\right)-2\left(\frac{R_{in}}{R_{out}}\right)^{\frac{3}{2}}\right], \quad (2.38)$$

where for an infinite disk, Eq. (2.38) becomes:

$$L_{disk\,\infty} = \frac{GMM_{dot}}{2R_{in}}. \quad (2.39)$$

Considering Eq. (2.39), the disk's luminosity depends on the disk's mass accretion rate. The equations deceivingly look like they are also mass dependent; however, by considering the definition of the ISCO, R_{in}, given by Eq. (2.28), and the definition of R_g, Eq. (2.29), there is no mass dependency, but the luminosity does depend on the parameter x.

The Efficiency of the Disk

In this section, we look to determine the efficiency of an accretion disk in the case of an infinite disk. Eq. (2.38) gives the total luminosity of an accretion disk. By substituting in the value of R_{in}, defined by Eq. (2.28), another way of expressing this luminosity is then:

$$L_{disk} = \frac{GMM_{dot}}{2\left(\frac{GM}{c^2}\right)}\left[1 - 3\left(\frac{R_{in}}{R_{out}}\right) - 2\left(\frac{R_{in}}{R_{out}}\right)^{\frac{3}{2}}\right] = \frac{M_{dot}c^2}{2x}\left[1 - 3\left(\frac{R_{in}}{R_{out}}\right) - 2\left(\frac{R_{in}}{R_{out}}\right)^{\frac{3}{2}}\right]. \quad (2.40)$$

By introducing a new parameter, η, for the accreted mass-to-energy efficiency of an accretion disk, we find η to be:

$$\eta = \frac{1}{2x}\left[1 - 3\left(\frac{R_{in}}{R_{out}}\right) - 2\left(\frac{R_{in}}{R_{out}}\right)^{\frac{3}{2}}\right], \quad (2.41)$$

where for the case of the infinite disk, η becomes:

$$\eta = \frac{1}{2x}, \quad (2.42)$$

so that the total luminosity of an infinite disk is:

$$L_{disk\,\infty} = \eta M_{dot}c^2. \quad (2.43)$$

The efficiency of the disk η is inversely proportional to x, which was earlier defined as the ratio between the ISCO and the gravitational radius of the disk. This ratio depends on whether the SMBH is rotating. Since we only consider the case for a non-rotating SMBH, this ratio is fixed with x = 6. Substituting this into the equation for η shows the efficiency to be:

$$\eta = \frac{1}{2(6)} \approx 0.083. \quad (2.44)$$

Since this is constant for the case of a non-rotating SMBH, the luminosity of an infinite accretion disk is only dependent on the mass accretion rate, M_{dot}, as shown below:

$$L_{disk} \propto M_{dot}. \tag{2.45}$$

Eddington Luminosity

Here, we introduce Eddington's Luminosity for an accretion disk. The Eddington Luminosity is the maximum luminosity an accretion disk can take while remaining in hydrostatic equilibrium. To derive the Eddington Luminosity, we begin with the radiation pressure gradient under the conditions of blackbody radiation and local thermodynamic equilibrium (LTE) over all emitted wavelengths (Carroll & Ostlie, 2018):

$$\frac{dP_{rad}}{dr} = -\frac{\bar{\kappa}\rho}{c} F_{rad}, \tag{2.46}$$

where P_{rad} is the radiation pressure, F_{rad} is the radiative energy flux defined by Eq. (2.47), and $\bar{\kappa}$ is an approximately wavelength-averaged opacity. Opacity measures a medium's ability to absorb electromagnetic radiation of wavelength λ per unit mass of the medium (Carroll & Ostlie, 2018). In this case, the medium is an accretion disk since the emitted light must pass through the disk to be seen by the observer, and the opacity units are m^2 km^{-1}. From Eq. (2.21) and the Stefan-Boltzmann Law, the radiative energy flux is then:

$$F_{rad} = \frac{L}{4\pi r^2}, \tag{2.47}$$

where L is the total luminosity emitted from the matter or the accretion disk. Substituting this definition for F_{rad} into Eq. (2.46), the radiation pressure gradient is then:

$$\frac{dP_{rad}}{dr} = -\frac{\bar{\kappa}\rho}{c}\frac{L}{4\pi r^2}. \tag{2.48}$$

Under the conditions of hydrostatic equilibrium, the pressure gradient required to counteract the gravitational force is (Carroll & Ostlie, 2018):

$$\frac{dP}{dr} = -\frac{GM\rho}{r^2}. \tag{2.49}$$

To find the Eddington luminosity, we equate the pressure gradient required under the conditions for hydrostatic equilibrium and the radiation pressure gradient defined in Eq. (2.48). The luminosity L is now set to give the Eddington Luminosity L_{edd}, which is then:

$$L_{edd} = \frac{4\pi GMc}{\bar{\kappa}}. \tag{2.50}$$

Returning to the discussion of opacity, we now discuss the interactions of light with the gas that forms the accretion disk. When light interacts with the particles in the disk, there are four possible types of interactions: 1) bound-bound transitions, 2) bound-free absorption, 3) free-free absorption, and 4) electron scattering (Carroll & Ostlie, 2018). For suitably high temperatures, the gas of the accretion disk, assumed to be comprised predominantly of hydrogen and helium, is ionized; therefore, electron scattering becomes the primary source of opacity. From Eq. (2.50) the maximum value of L_{edd} will occur for the smallest value of $\bar{\kappa}$. By setting $\bar{\kappa} = \kappa_{es}$ gives the smallest opacity possible for ionized gas, yielding the maximum value in L_{edd} for a given mass M of the SMBH.

The electron scattering opacity κ_{es} for our accretion disk is then:

$$\kappa_{es} = \frac{\sigma_{es}}{\mu_e m_H}, \tag{2.51}$$

where σ_{es} is the electron scattering cross-section (defined by Eq. (2.58), with the discussion to follow), μ_e is the mean molecular weight per electron, and m_H is the mass of a hydrogen atom, whose value can be found in Table 7.1. The values of μ_e and σ_{es} used in this work are detailed below. The mean molecular weight per electron can be approximated as (Carroll & Ostlie, 2018):

$$\mu_e \approx \frac{2}{1+X} \approx 1.2, \tag{2.52}$$

where X = Hydrogen mass fraction, where in this paper, we use the approximated value of the hydrogen mass fraction to be $X \approx 0.7$. The electron scattering cross-section is then given by:

$$\sigma_{es} = \frac{8\pi}{3}\left(\frac{1}{4\pi\varepsilon_0}\right)^2\left(\frac{e^2}{m_e c^2}\right)^2 = 6.65246 \times 10^{-29}\, m^2, \tag{2.53}$$

where ε_0 is the permittivity of free space, m_e is the mass of an electron, and e is the electronic charge. All three values can be found in Table 7.1.

Then by substituting Eq. (2.51) into Eq. (2.50), the Eddington luminosity can now be expressed as:

$$L_{edd} = \frac{4\pi GMc(\mu_e m_H)}{\sigma_{es}}. \tag{2.54}$$

One beneficial application of the Eddington luminosity is the ratio between the total disk luminosity and the Eddington luminosity. For simplicity, we use the total luminosity of an infinite disk in the form of Eq. (2.43), such that the Eddington luminosity ratio is then:

$$\frac{L}{L_{edd}} = \frac{L_{disk\ (infinite)}}{L_{edd}} = \frac{\eta M_{dot} c\sigma_{es}}{4\pi GM\mu_e m_H}. \tag{2.55}$$

This ratio is used as a limiting factor for models of accretion disks where the upper and lower bounds of the limit are 1 and 0.01, respectively. Outside of both bounds, the accretion mode, structure, radiative properties, and the structure of the accretion are expected to change radically compared to the model we are exploring here.

2.2 The Model

A Brief Description of the Model

We used a Microsoft Excel ® spreadsheet to compute the fundamental properties of an accretion disk. The model requires the user to set specific input parameters. It then computes the fundamental properties, such as the disk's temperature, radiative flux, and luminosity, as just a few examples.

The model is scaled against the radial position in the disk, r. The scale was built using the outer radius corresponding to a fixed minimum temperature to set the step size, $d\log_{10}\left(\frac{r}{R_{in}}\right)$. The model then used the equations derived in the previous section to build graphs that contain the key information of an accretion disk under the standard model assumptions previously stated, most of which were plotted vs. the radial position in the disk. These results will be analyzed in the following sections and discussed.

Input and Output Parameters

The model requires the user to set specific input parameters for the disk, which are: 1) the mass of the SMBH M, 2) the mass accretion rate of the accretion disk M_{dot}, 3) the Eddington Luminosity Ratio L/L_{edd}, 4) the ratio between the ISCO and the gravitational radius x, and 5) the outer radius of the disk (defined as the point at which the temperature in the disk reaches 2000 K).

Four models with pre-selected input values have been chosen and are outlined in Table 2.1. For each of the four models (A, B, C, and D), there are several calculated output values of interest in addition to the input parameters described above. These output values have also been included in Table 2.1 and are listed below with reference to the appropriate derived equation(s).

- The gravitational radius, R_g: Eq. (2.29)
- The ISCO, R_{in}: Eq. (2.28), which in this model essentially sets the disk efficiency, η: Eq. (2.42)
- The characteristic temperature of the disk, T_{disk}: Eq. (2.30)
- The maximum temperature of the disk T_{max}: Eq. (2.35)
- The fully integrated finite luminosity of the disk, L_{disk}: Eq. (2.38)
- The fully integrated infinite luminosity of the disk $L_{disk\ (infinite)}$: Eq. (2.39)
- The Eddington luminosity L_{edd}: Eq. (2.54)

Additionally, two parameters were also collected from the disk itself. Those were the disk's maximum temperature and the disk's total luminosity. The total luminosity of the disk is comparable to the analytical finite disk luminosity found by performing a Riemann Sum over the entire disk. Both parameters are given in Table 2.1 for each of the four models.

	Parameter	Units	A	B	C	D
Input Parameters	M	10^8 $M_\odot$	1	10	1	3
	$\frac{L}{L_{edd}}$		0.1	0.1	0.3	$0.0\dot{3}$
	M_{dot}	$M_\odot$ yr^{-1}	0.314	3.14	0.941	0.314
	$R_{out\ (T=2000K)}$	10^{14} m	3.26	15.1	4.69	4.69
	x	$\frac{r}{R_g}$	6	6	6	6
Calculated Output Values	R_g	10^{11} m	1.48	14.8	1.48	4.43
	R_{in}	10^{11} m	8.86	88.6	8.86	2.66
	η		0.0833	0.0833	0.0833	0.0833
	T_{disk}	10^5 K	1.6785	0.94386	2.2090	0.96905
	T_{max}	10^4 K	8.189	4.605	10.78	4.728
	L_{disk}	10^{38} W	1.4689	14.577	4.4162	1.4584
	$L_{disk\ (infinite)}$	10^{38} W	1.4797	14.797	4.4391	1.4797
	L_{edd}	10^{38} W	14.797	147.97	14.797	44.391
Collected Output Values	T_{max}	10^4 K	8.189	4.605	10.78	4.728
	L_{disk} (Riemann Sum)	10^{38} W	1.4681	14.551	4.4148	1.4559

Table 2.1 – A table of the input parameters, calculated output values, and collected output values for each of the four models (A, B, C, and D) that will be analyzed in this paper. Each parameter is color coded to match the graphs to be shown in the coming sections.

2.3 Results

Discussion of Output Values

Here we will analyze the collected output parameters with the calculated output parameters for the four models. The values are given in Table 2.1, and for the purposes of this analysis and further discussions, we will consider model A to be the standard model on which we base our comparisons. First, we will compare the output values for the maximum temperature of the disks and, second, the different output values relating to the luminosity of the disk.

Comparing the values of T_{max} collected from the model to those calculated, we find that the two values for each of the four models agree. Equation (2.35) shows that the maximum temperature of the disk is approximately half the characteristic temperature of the disk. Observing the values state in Table 2.1 for the characteristic temperature of the disk shows this to be true for each of the four models. Additionally, comparing the values for the four models, the maximum temperature varies with a change in mass M, and mass accretion rate M_{dot} as:

$$T_{max} \propto T_{disk} \propto \frac{{M_{dot}}^{\frac{1}{4}}}{M^{\frac{1}{2}}}. \tag{2.56}$$

These relationships are observed in the values of T_{disk} and T_{max}, in that Models B and D, which have more massive SMBHs than Model A, have cooler accretion disks (calculated values of T_{disk} and T_{max}). Model B experiences two competing functions, with an increase in mass but also an increase in mass accretion rate; however, the change in mass has a more significant impact. Model C has the highest maximum temperature since the mass was not changed from Model A's, but the mass accretion rate was increased.

There were four different luminosities detailed in Table 2.1. Three were calculated: the total luminosity of a finite disk, an infinite disk, and the Eddington luminosity. The total luminosity of each disk model was also collected by performing a Riemann Sum over the luminosity at every annulus. As expected, the infinite disk luminosity calculated is larger than the finite disk luminosities (L_{disk} and $L_{disk\ (Riemann\ Sum)}$) by a small factor. It will be shown in the following graphs that the inner region of the accretion disk contributes the most to the total

luminosity of the accretion disk; therefore, we expect the difference in total luminosity from the finite disk to the infinite disk to be small.

The two values for the fully integrated luminosity of a finite disk (L_{disk} and $L_{disk\ (Riemann\ Sum)}$) agree within three significant figures across all four models; therefore, the difference is almost negligible. The luminosity given by performing a Riemann Sum over the disk is consistently lower than the calculated luminosity for each of the four models. This difference can be explained since the Riemann Sum is only an approximation, and without an infinitely small step size, it is expected there to be some discrepancy between the calculated and estimated values.

Presentation of Findings

In this section, five graphs are presented that outline the fundamental properties of the structure of standard model accretion disks. On each graph are plotted the four models whose input parameters are defined in Table 2.1. As mentioned, model A will be taken as the standard model, of which the other models will be compared. The graphs, which are plotted as functions of radius, have been plotted against the radial position defined by the ratio of the physical radius r to the gravitational radius R_g: r/R_g. This choice was made so that each of the four models could be easily compared on the same scale. The physical position of the ISCO depends on the SMBH's mass around which the accretion disk is located shown by Eq. (2.28) and Eq. (2.29). Therefore, changing the SMBH mass will shift that model's position on the graph, making it difficult to compare to other models. We chose to remove this additional factor and complication by presenting the results on a dimensionless scale, r/R_g.

Figure 2.3 is a graph of the fully integrated luminosity of a finite disk vs. the ratio of the fully integrated infinite disk luminosity and the Eddington luminosity ratio. This graph shows the range of disk luminosities possible for three characteristic masses of SMBHs in AGN (10^7 $M_\odot$, 10^8 $M_\odot$, and 10^9 $M_\odot$), between the bounds of the Eddington luminosity ratio, is 10^{36} W and 10^{40} W. Three straight lines represent these ranges since both the infinite and finite disk luminosities are independent of the mass, and the Eddington luminosity scales directly to M, as can be seen in Eq. (2.54). The graph also displays the four models being considered in this paper. Their fully

integrated disk luminosities can be determined, and they all lie well within the boundaries of the Eddington luminosity ratio.

Figure 2.4 is a graph of the effective temperature of the disk vs. the dimensionless radius scale, r/R_g for the four models, A, B, C, and D. The equation for the effective temperature is given by Eq. (2.26), which shows the following power relations for the mass of the SMBH, the mass accretion rate, and the radial component, for the case that $r >> R_{in}$, to be:

$$T_{eff}(r) \propto \frac{M_{dot}^{\frac{1}{4}}}{M^{\frac{1}{2}}}\left(\frac{R_{in}}{r}\right)^{\frac{3}{4}}. \tag{2.57}$$

We, therefore, observe that for a fixed mass but a change in M_{dot}, and by default, a change in L/L_{edd}, the temperature scales to $M_{dot}^{1/4}$. This can be observed in the difference between the graph for Model A, and C. Model C has a higher mass accretion rate and, therefore, a higher effective temperature. It, in fact, has the hottest disk of the four models because it also has the lowest mass. Eq. (2.57) shows that for a fixed M_{dot}, the effective temperature scales to $M^{-1/2}$; therefore, the more massive the SMBH, the cooler the accretion disk (within the limits of L/L_{edd} for the mass accretion rate). This can be seen in Figure 2.4, where the plots for Models B and D lie below the less massive Models (A and C). It can also be seen from Model B, which in comparison to Model A, experiences both a change in M and M_{dot}, that these two parameters act as competing functions.

Other observations from Figure 2.4 include that the inner region of the disk is the main contributor to the disk's temperature, with the temperature increasing initially, until reaching the point in the disk where $r = 49/6\ R_g$. This is the point at which the maximum temperature of the disk is located. The temperature then decreases with radius as $r^{-3/4}$, as shown in Eq. (2.57). This power law is only an approximation for the fall-off rate of the effective temperature because the disk does not extend to an infinite radius. At very small values of R_{in}/r, the power law very nearly approaches the value of -3/4, but only a disk at an infinite radius would ever equal this value. This power law is, therefore, an asymptotic relation. The final observation to be made is that Figure 2.4 demonstrates that the minimum temperature of the disk is fixed to a value of ~ 2000K, which is responsible for setting the outer radius of the disk.

Figure 2.5 is a graph of the radiative flux of the disk vs. the dimensionless radius scale, r/R_g for the four models of accretion disks outlined in Table 2.1. Since, by Eq. (2.9), the radiative flux is directly proportional to the effective temperature to the fourth power ($T_{eff}(r)^4$), this graph varies with the input parameters as described in Figure 2.4, but with the following power relations to the mass of the SMBH, the mass accretion rate, and the radial component, for the case that $r >> R_{in}$:

$$F \propto \frac{M_{dot}}{M^2}\left(\frac{R_{in}}{r}\right)^3. \tag{2.58}$$

Additionally, the graph shows the ranges of radiative flux from the different models and that the main contribution is from the inner regions of the disk. From the point of maximum radiative flux, the amount of radiative flux falls off approximately at a rate of radius to the negative third power (r^{-3}). As mentioned for the fall-off rate of the effective temperature of the disk, the power relation is only an approximate estimation because the slope of the line on the log-log plot would only ever reach r^{-3} power for the case of an infinite disk and is, therefore an asymptotic relation.

Figure 2.6 is a graph of the differential disk luminosity vs. the dimensionless radius scale, r/R_g for the four models (A, B, C, and D) with input values defined in Table 2.1. The equation for the differential luminosity of the disk is given by Eq. (2.23), which, when the values of T_{eff} and T_{disk} are substituted into the equation, shows the following power relations for the mass accretion rate, and the radial component, for the case that $r >> R_{in}$, to be:

$$dL(r) \propto \frac{M_{dot}}{r}. \tag{2.59}$$

The direct proportionality to the mass accretion rate is demonstrated in Figure 2.6 by the difference in the four models where Model B, which has the highest M_{dot} value, is also the most luminous disk. This is true for the other models as well; however, it can be seen that although Model A and Model D have the same value for M_{dot}, their graphs look very slightly different. Because they have the same value of M_{dot}, their total disk luminosities will remain the same; however, due to their difference in mass, the position of the contributions to the luminosity of the disk will differ. Figure 2.6 also shows that the main contribution to the luminosity of the disk is the inner region of the disk. After the maximum luminosity is reached, the luminosity decreases with radius as shown in Eq. (2.59).

Figure 2.7 is a graph of the ratio between the cumulative luminosity at each annulus r and the fully integrated luminosity of the disk gathered by performing a Riemann Sum vs. the dimensionless radius scale, r/Rg. The four models are graphed; however, they follow the same path, so the graph can be seen to overlap. The only changes between the four modes are the value of the ratio at the ISCO and the final position in r/R_g space. The most interesting information that can be gained from this plot is where most of the power in an accretion disk is located. The very steep initial increase in this ratio signifies that the inner region of the disk contributes a significant fraction of the power of AGN accretion disks (for a variety of input parameters). Approximately 90% of the total power from an accretion disk comes from within $r = 100\ R_g$, demonstrating that the contributions from the outer portion of the disk are minimal.

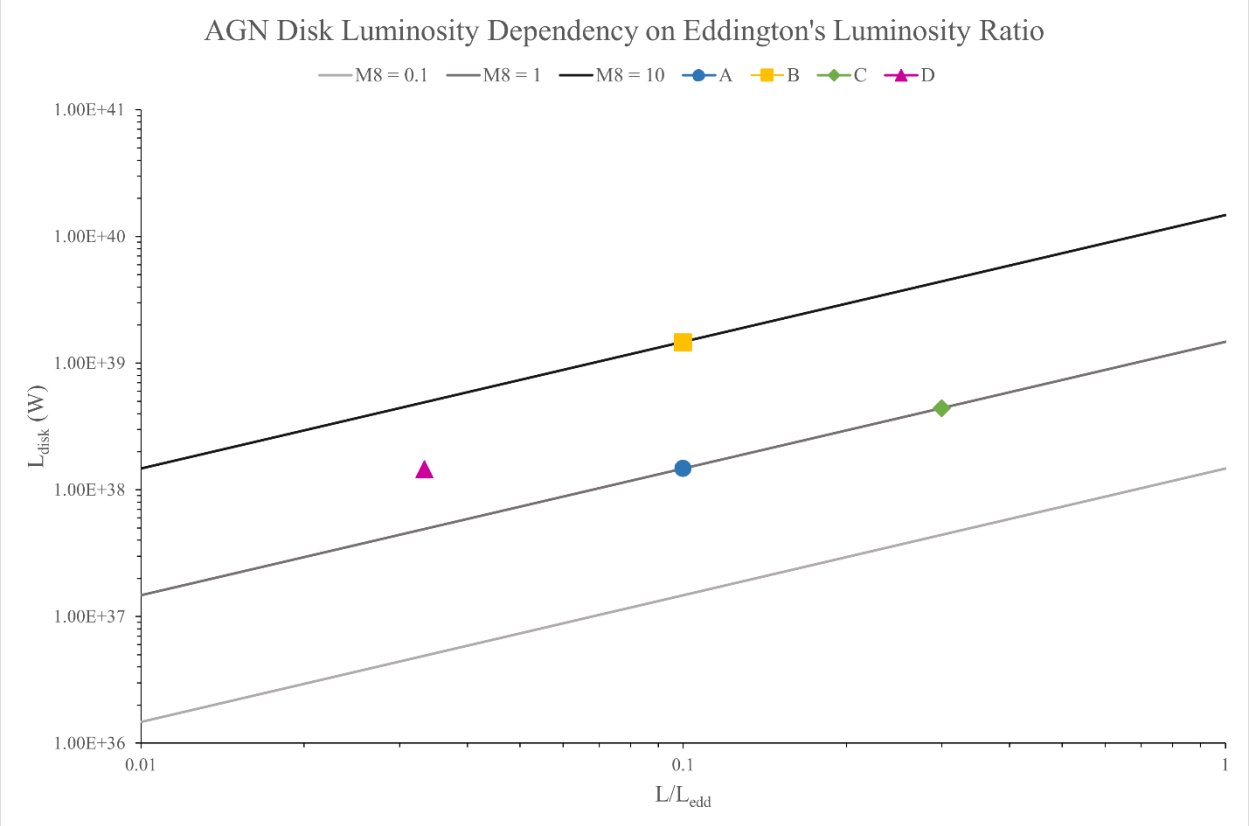

Figure 2.3 – This is a graph of the fully integrated luminosity of an accretion disk vs. the Eddington luminosity ratio. This demonstrates the range in possible fully integrated luminosities for three typical masses of SMBHs in AGN accretion disks (10^7 $M_\odot$, 10^8 $M_\odot$, and 10^9 $M_\odot$ - denoted in the legend as M8 = 0.1, 1, and 10 respectively). The four models evaluated throughout this paper are shown to lie well within the bounds for the Eddington luminosity ratio.

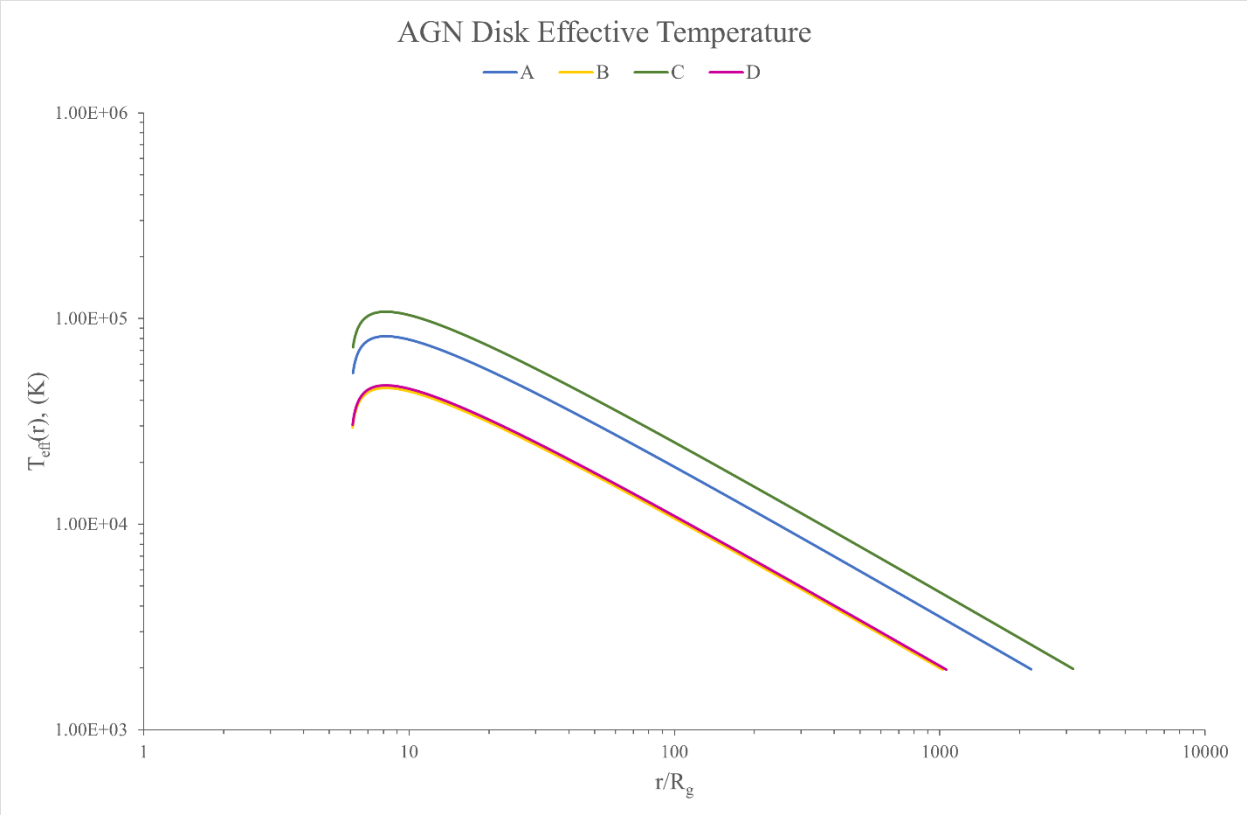

Figure 2.4 – This is a graph of the effective temperature of the disk vs. disk radius in units of r/R_g. The graph shows that the main contribution to the temperature of the disk comes from the disk's inner region, and that after the maximum temperature is reached, the temperature decreases with radius until reaching the minimum temperature (T = 2000 K) defining the outer radius of the disk. Note that Models B and D are nearly coincident.

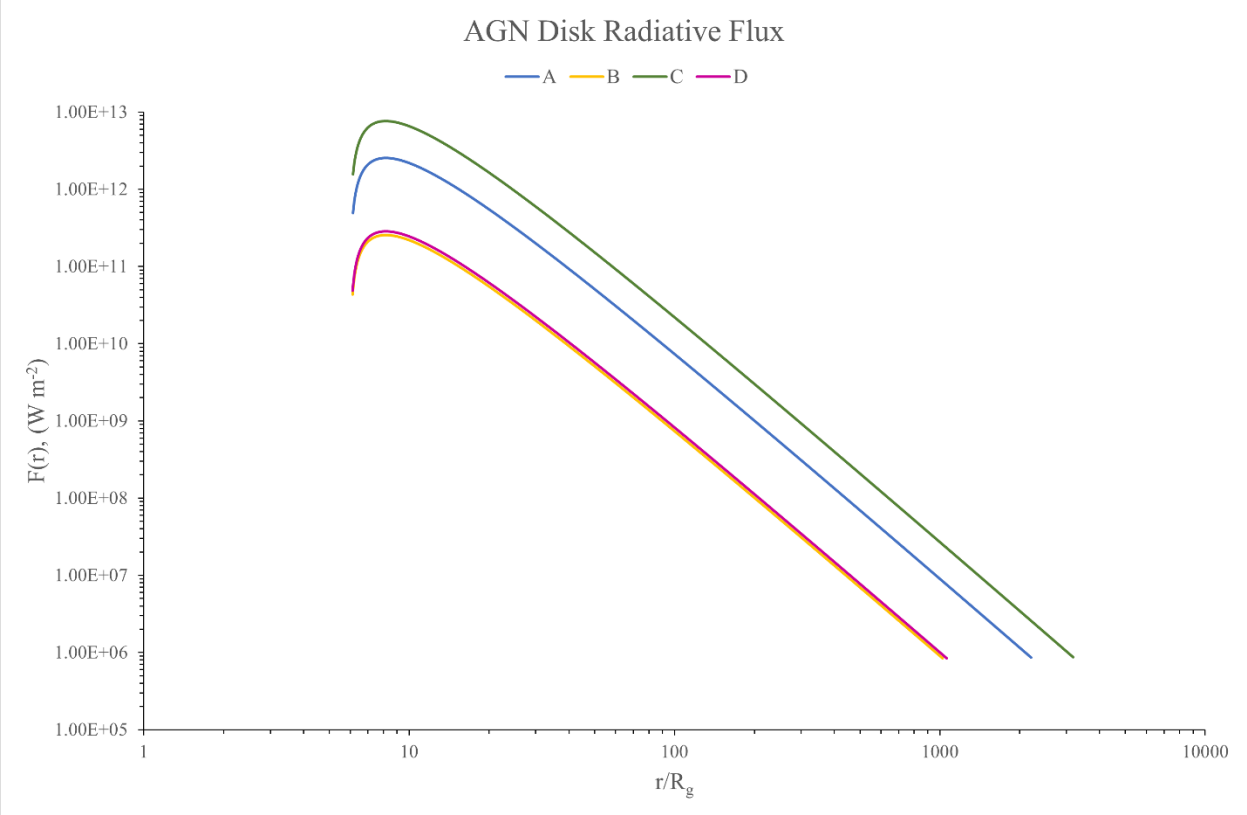

Figure 2.5 – This is a graph of the radiative flux of the disk vs. disk radius in units of r/R_g. Eq. (2.9) demonstrates how the radiative flux scales with temperature to the fourth power through the accretion disk.

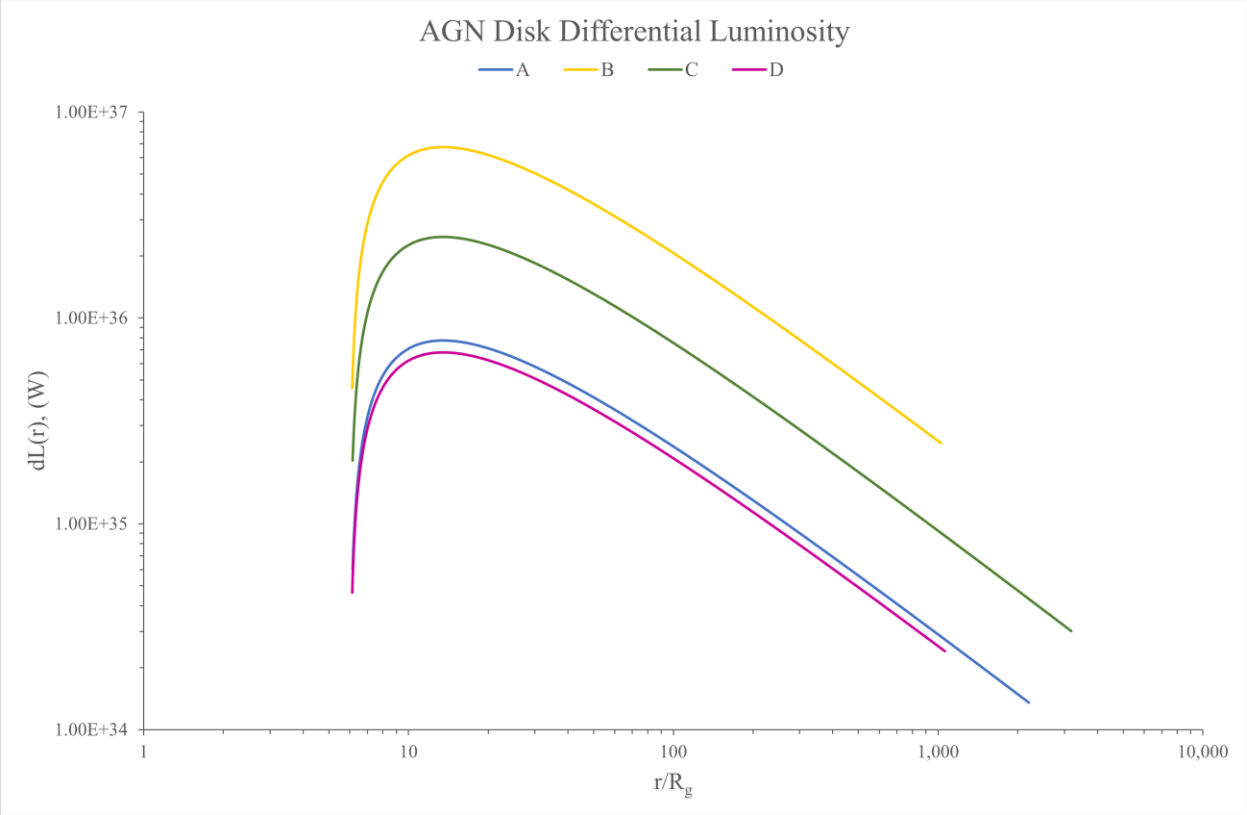

Figure 2.6 – This is a graph of the differential luminosity at each annulus of the disk vs. disk radius in units of r/R_g. The graph shows the main contribution to the luminosity of the disk is from the inner region (see Eq. (2.23) for the relation between the differential luminosity and the effective temperature).

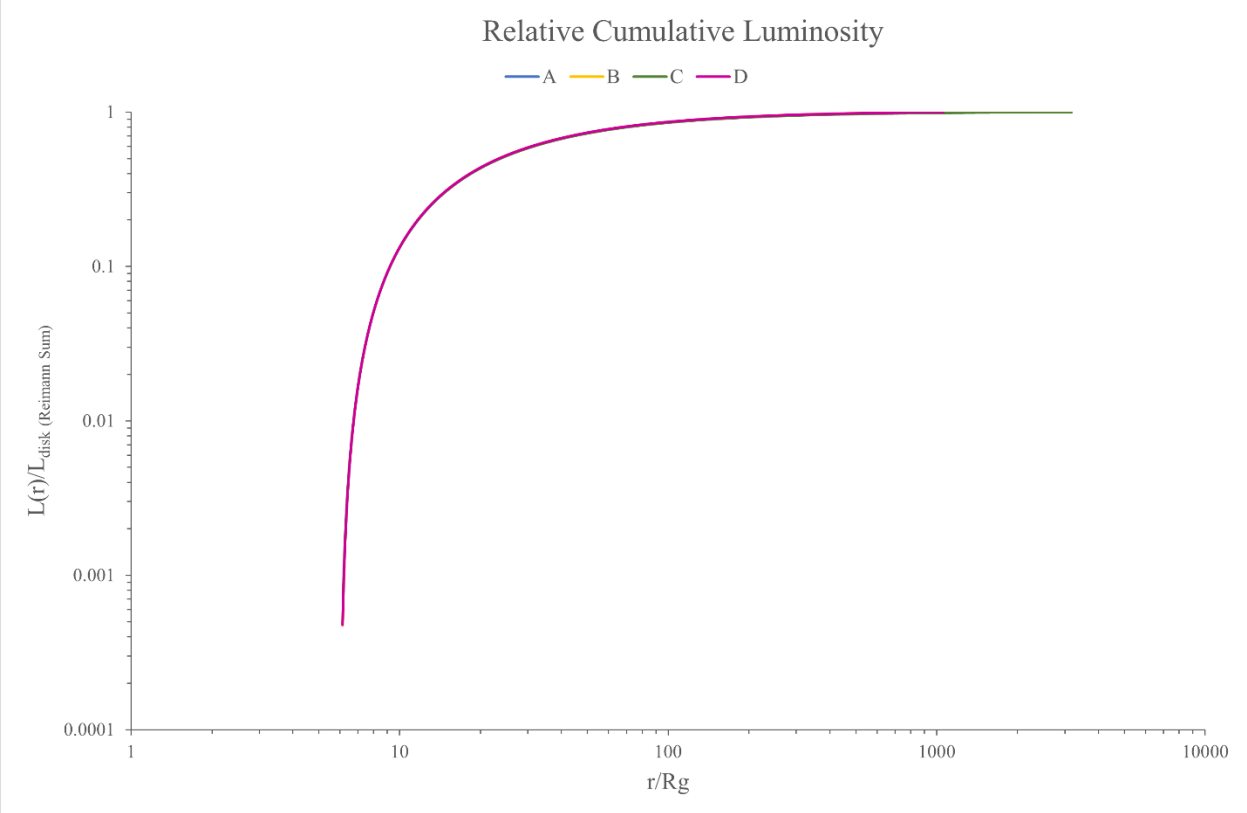

Figure 2.7 – This is a graph of the ratio of the disk's cumulative luminosity, as integrated outward from the ISCO, to the total luminosity of the disk vs. the disk's radius in units of r/R_g. This demonstrates that most of the power emitted from AGN accretion disks are located in the inner few 10s of gravitational radii, with approximately 90% emerging from the inner 100 R_g.

3. Accretion Disk Spectrum

3.1. Physical Considerations

This section continues from Section 2.1, where the necessary derivations for blackbody radiation, temperature, radiative flux, and luminosity were derived. Here we will discuss the additional derivations required to model the spectrum of a standard model accretion disk.

The Spectrum L_λ vs. λ

To obtain a spectrum of the standard model accretion disk under the assumptions discussed previously, we find the specific luminosity per unit wavelength L_λ by summing over the contributions from all annuli in the disk for wavelengths spanning 1 nm to 10^4 nm. Recalling from Eq. (2.21) and the Stefan-Boltzmann Law, the differential specific luminosity can be written as:

$$dL_\lambda = F_\lambda dA, \tag{3.1}$$

where dA is the differential surface area of the two-sided accretion disk given by Eq. (2.22), and F_λ is the surface specific flux per unit wavelength, given by Eq. (2.7) for the outward hemisphere. Since the accretion disk is two-sided, the total surface flux is twice that of Eq. (2.7), and hence by evaluating the integral given in Eq. (2.7), F_λ is then:

$$F_\lambda = \pi B_\lambda(T), \tag{3.2}$$

where $B_\lambda(T)$ is Planck's function for blackbody radiation at radius r given by Eq. (2.5). To find the specific luminosity at each annulus, dL_λ, we substitute Eq. (3.2) and Eq. (2.22) into Eq. (3.1) which is then:

$$dL_\lambda = 4\pi^2 r B_\lambda(T) dr. \tag{3.3}$$

The area integrated specific luminosity is then:

$$L_\lambda = 4\pi^2 \int_{R_{in}}^{R_{out}} r B_\lambda(T) dr\,, \tag{3.4}$$

where R_{in} and R_{out} are the ISCO and the outermost radius, respectively. In computing the spectrum L_λ, we consider wavelengths spanning $1\ nm \leq \lambda \leq 10^4\ nm$ which was deemed to be

an appropriate range to cover the wavelengths that contribute with any significance to the observed spectrum fo AGN, and in consideration of the values of the disk temperature considered here: $2000 \leq T(K) \leq 200{,}000$.

Rayleigh-Jeans Tail Approximation

Rayleigh-Jeans law (Eq. 3.5) was first proposed before establishing the Planck function for blackbody radiation (Carroll & Ostlie, 2018). Lord Rayleigh sought an expression that accounted for the blackbody radiation curve; however, what he found is now known as the 'ultraviolet catastrophe' because the function would approach infinity for very short wavelengths as can be seen by the following equation which gives Rayleigh-Jeans law:

$$F_\lambda = \frac{\pi hckT}{\lambda^4}. \tag{3.5}$$

His result, however, is in excellent agreement with the tail of the blackbody function at long wavelengths, where:

$$\frac{hc}{\lambda} \ll kT. \tag{3.6}$$

Therefore, we have used the result from Rayleigh-Jeans law to approximate the remainder term of the total luminosity of the disk when a Riemann sum was found over the spectrum of the disk. A correction is necessary because our model only evaluates the wavelengths within the range $1\ nm \leq \lambda \leq 10^4\ nm$, but the fully integrated luminosity of the disk L_{disk} is found by integrating over all wavelengths:

$$L_{disk} = \int_0^\infty L_\lambda \, d\lambda\,, \tag{3.7}$$

The last point in our spectrum L_λ as summed over all annuli, is well approximated to lie on the Rayleigh-Jeans tail. Since our model does not extend to $\lambda \rightarrow \infty$, only to $\lambda = 10^4$ nm, there is non-negligible light that lies within the Rayleigh-Jeans tails of the cooler blackbodies in our disk that extend beyond 10^4 nm. To account for this discrepancy, the following approximation was then added to the result of the Riemann sum over L_λ ($1 – 10^4$ nm) to obtain L_{disk}:

$$L_{remainder} \approx \frac{1}{3}[\,\lambda L_{\lambda}(10^4\ nm)]. \tag{3.8}$$

3.2. The Model

A Brief Description of the Model

We molded the accretion disk spectrum in a spreadsheet to model the spectrum, where the user sets several input parameters, similar to the disk structure model previously discussed. The radial position scale was used directly from the disk structure model, as were the effective temperature and area elements needed to build the spectrum. The initial and final wavelengths considered in computing the spectrum were 1 nm and 10^4 nm respectively, and the step size in wavelength, dlogλ, was chosen to be 0.0025. The results of this model will be outlined and discussed in the following sections.

Input and Output Parameters

The input parameters required for this model are the same as those previously discussed in Section 2.2 for the disk structure model. The analysis of the results in this section use the same four models (A, B, C, and D) discussed in Section 2 will also be applied to the results here. Their input values were previously stated in Table 2.1; however, they will be restated in Table 3.1.

The output parameters found from the model for the spectrum of the disk are: 1) the total luminosity of the disk $L_{\text{disk Riemann Sum}}$, 2) the luminosity of the disk integration over 1 nm to 91.20 nm which will be referred to as $L_{\text{disk ion}}$, and 3) the wavelength of maximum blackbody intensity for the highest temperature in the disk $\lambda_{\text{max (Tmax)}}$. The total luminosity of the disk was found by performing a Riemann Sum over the total contributions over all wavelengths as shown above. The hydrogen Lyman-Limit is the ionization energy required to remove an electron from the ground state of hydrogen. The ionization energy is 13.6 eV which corresponds to a photon of wavelength ~ 91.20 nm (Carrol & Ostlie, 2018). A Riemann Sum was performed from the initial wavelength (1 nm for this model) up to the Lyman-Limit wavelength to acquire the output values of $L_{\text{disk ion}}$ for each of the four models. Finally, Wien's law, given by Eq. (2.11), was used to find the wavelength at the peak of the blackbody function for the highest temperature in the disk.

	Parameter	Units	A	B	C	D
Input Parameters	M	10^8 $M_\odot$	1	10	1	3
	$\frac{L}{L_{edd}}$		0.1	0.1	0.3	$0.0\dot{3}$
	M_{dot}	$M_\odot$ yr^{-1}	0.314	3.14	0.941	0.314
	$R_{out\ (T=2000K)}$	10^{14} m	3.26	15.1	4.69	4.69
	x	$\frac{R_{in}}{R_g}$	6	6	6	6
Output Parameters	L_{disk} Riemann Sum	10^{38} W	1.4681	14.551	4.4148	1.4559
	$L_{disk\ ion}$	10^{38} W	0.71477	3.1354	2.6709	0.33061
	$\lambda_{max\ (Tmax)}$	nm	35.39	62.93	26.89	61.29

Table 3.1 – A table of the input parameters and output values for each of the four parameters that will be analyzed in this paper. Each parameter is color coded to match the graphs to be shown in the coming sections.

3.3. Results

Discussion of Output Values

Here we will analyze the collected output parameters detailed in Table 3.1 for the four models. The total luminosity of the disk given by the Riemann Sum over the spectrum of the disk is found to equal the Riemann Sum found from the model of the disk structure. That is, when comparing the values of the $L_{\text{disk Riemann Sum}}$ from Table 3.1 with the values from Table 2.1 for the four models, they are found to be equal.

The contribution to the luminosity from the disk wavelengths shorter than the Lyman-Limit is detailed in Table 3.1. The total contributions vary from approximately 20% to 60% of the total luminosity of the disk given by the Riemann Sum. The percentage of the total contribution from the shorter wavelengths is greater for hotter disks, with the contribution for Model C, the hottest of the four disks considered, to be approximately 60%. Finally, we list the values of the wavelength $\lambda_{\text{max (Tmax)}}$, where the blackbody function peaks for the maximum temperature in the disk.

Presentation of Findings

This section presents two graphs and a table of values from the second graph, which describe the contributions to the spectrum from the disk and the spectra for our four model accretion disks.

Figure 3.1 illustrates the contribution functions to the specific luminosity L_λ in the disk for ten different wavelengths: a graph of the differential specific luminosity, dL_λ, and the dimensionless radius scale, r/R_g for Model A. The ten selected wavelengths were chosen as multiples of the wavelength corresponding to the Hydrogen Lyman-Limit (91.20 nm), to show a variety of wavelengths considered in the spectrum. Since our model grid contains a finite number of steps in wavelength, the wavelength values listed in Figure 3.1 are the closest values possible to the multiples of 91.20 nm. The graphs of dL_λ vs. r/R_g corresponding to Models B, C, and D can be found in the Appendix (Figure 7.1, 7.2, and 7.3, respectively).

As demonstrated in Figure 2.4 the effective temperature of an AGN accretion disk reaches a maximum near a radius of about $8R_g$ and then decreases with radius. From our discussion on blackbody radiation in Section 2.1, we know that a hotter blackbody emits a greater radiative flux and peaks at shorter wavelengths. Figure 2.2 demonstrates that blackbodies emit very little light shortward of their wavelengths of maximum intensity. We see in Figure 3.1 that the shorter wavelengths in the observed spectrum are largely confined to arise and peak within inner regions of the disk where the temperature is hotter, whereas longer wavelengths are emitted from a broader range in the disk and peak in their contributions from the outer disk where the temperature is cooler.

Figure 3.2 shows the spectra for the four disk models (A, B, C, and D) for input parameters defined in Table 3.1. The spectrum is a sum over the contributions (see Figure 3.1) from all the radii in the disk, and here we plot the quantity λL_λ vs. λ (rather than L_λ) to identify where most of the power in the spectrum resides. For example, any two spectra with the same maximum value in λL_λ will have the same luminosities L_{disk}. Models A and D share this characteristic, but Model D has a higher mass and thus a cooler disk so its spectrum peaks at a longer wavelength than that arising from Model A. Model B has the same T_{disk} as Model D and shows a similar shaped spectrum, but has a larger M_{dot}, and so is more luminous. Model C has a lower mass and a higher M_{dot} and so a greater T_{disk} than Model A. Thus, Model C is both more luminous and has a spectrum that peaks at shorter wavelengths than Model A. Table 3.1 gives the values in λL_λ for the ten wavelengths plotted in Figure 3.1 for each of the four models.

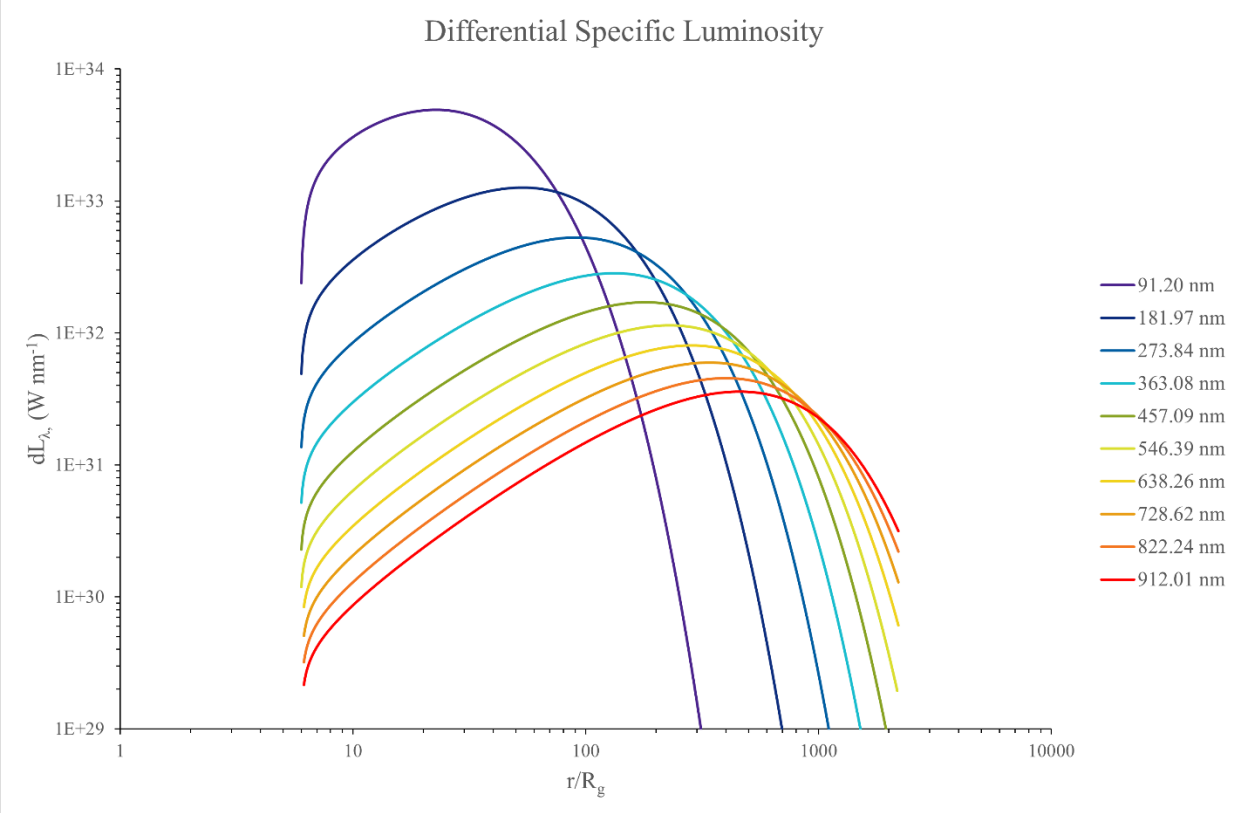

Figure 3.1 – A graph of the wavelength specific luminosity contributions over the disk for each of the ten wavelengths selected as scale factors of the Ionization Lyman-Limit for hydrogen at 91.20 nm. The graph is plotted for the input parameters for Model A only.

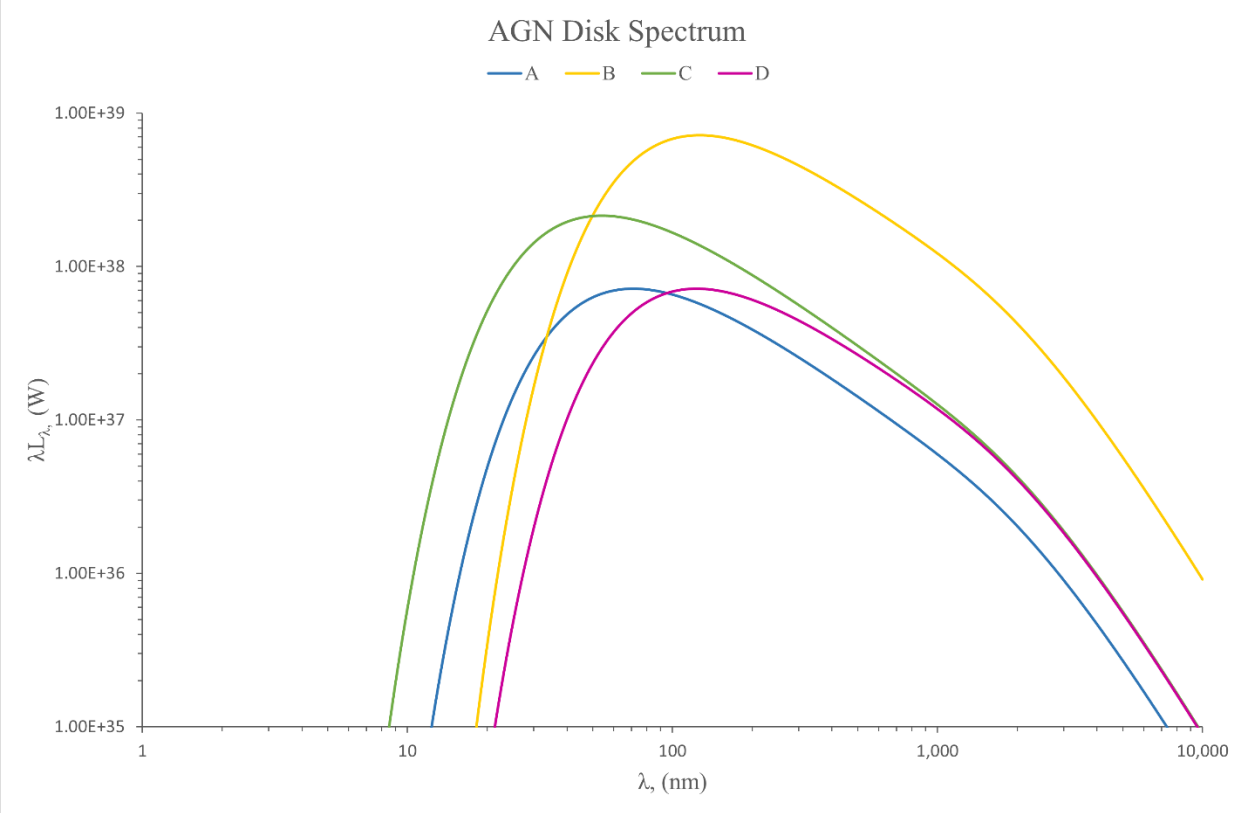

Figure 3.2 – A graph of the wavelength-multiplied specific luminosity vs. wavelength producing the spectrum of four accretion disks. The spectra plotted show the range of wavelengths contributing the most to the fully integrated luminosity in the disk.

λ (nm)	A λL_λ (10^{38} W)	B λL_λ (10^{38} W)	C λL_λ (10^{38} W)	D λL_λ (10^{38} W)
91.20	0.68230	6.4047	1.7749	0.65232
181.97	0.42427	6.4890	0.97264	0.64016
273.84	0.28155	4.9120	0.62319	0.48047
363.08	0.20598	3.8045	0.44884	0.37078
457.09	0.15768	3.0116	0.34037	0.29289
546.39	0.12745	2.4839	0.27354	0.24126
638.26	0.10552	2.0862	0.22551	0.20245
728.62	0.089594	1.7898	0.19090	0.17358
822.24	0.076957	1.5500	0.16358	0.15024
912.01	0.067368	1.3653	0.14293	0.13229

Table 3.2 – A table of values in λL_λ at particular wavelengths for the AGN disk spectra appearing in Figure 3.2. The models are color coded to match Table 3.1 and Figure 3.2.

4. Emission Disk Variability

4.1. Conceptual Discussion

A key characteristic of AGN accretion disks is that they are highly variable. There have been many attempts to formulate models which accurately explain their variability. However, there is no one model which fulfills every component of their variability. Formulating such a model is well beyond this project's scope; however, to acknowledge the highly variable nature of AGN, we discuss one of the many proposed models for variability and briefly discuss its theory.

Sun et al. (2020) propose a hot corona extending into the X-ray and far-UV range of the accretion disk. This corona is believed to produce magnetic fields which connect the thin accretion disk with the corona. Therefore, as the magnetic field produced by the corona fluctuates, these fluctuations propagate through the thin accretion disk, which drives temperature fluctuations within the disk. Figure 4.1 is an image of this model, presented in the Sun et al. paper (2020). We refer the reader to the original paper for a more detailed description and discussion of this model.

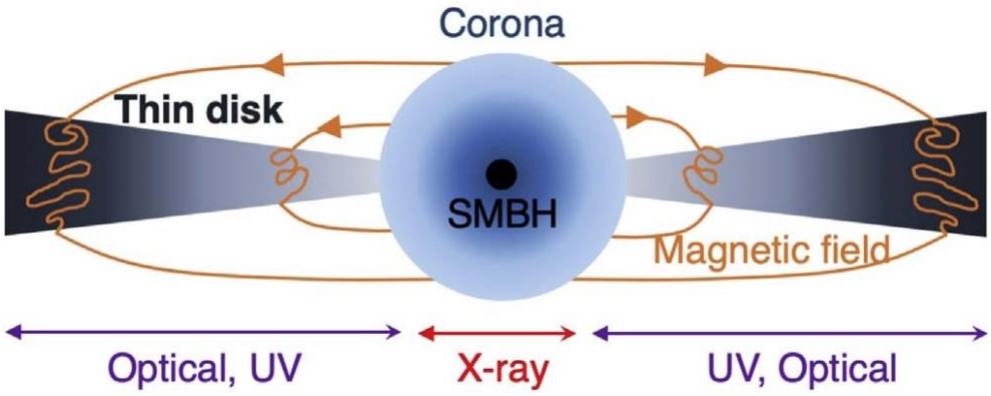

Figure 4.1 – A image of the model of AGN variability proposed by Sun et.al. The image shows the hot corona extending into the X-ray and far-UV range of the thin accretion disk around a SMBH. Magnetic fields produced by the corona are also depicted and show fluctuations occurring within the disk which are proposed to cause temperature fluctuations. Image Credit: (Sun et al., 2020)

4.2. The Model

A Brief Description of the Model

To simulate the variability of an accretion disk, we applied a simple condition to adjust the temperature distribution within the disk. A scale factor (T_{factor}) can be changed so that the effective temperature retrieved from the model of the disk structure is adjusted appropriately. This is a simple multiplicative factor, and the user sets how much of the disk this factor affects.

Input and Output Parameters

The input parameters additional to those required by the structure and spectrum models are: 1) the scale factor (T_{factor}) and 2) the outer boundary under which the scale factor is applied (Perturbation outer boundary). For the results discussed below, we perturbed the disk from the ISCO out to r = 400 R_g. The results below are for our standard chosen model (Model A) only and show the change in output values and the disk spectrum adjusted for the variability, identified as perturbed, and the standard values stated in Section 3.3, identified as unperturbed. Table 3.1 should be referenced for the input parameters specific to Model A.

			Model A	
	Parameter	**Units**	**Perturbed**	**Unperturbed**
Input Parameters	T_{factor}		1.2	
	Perturbation outer boundary	$\frac{r}{R_g}$	400	
Output Parameters	$L_{disk\ Riemann\ Sum}$	10^{38} W	2.9910	1.4681
	$L_{disk\ ion}$	10^{38} W	1.7297	0.71477
	$\lambda_{max\ (Tmax)}$	nm	29.49	35.39

Table 4.1 – A table of the input parameters and output values for the perturbed and unperturbed disks for Model A only. The text is color coded to match Figure 4.3 in the results section below.

4.3. Results

Discussion of Output Values

Here we will analyze the collected output parameters detailed in Table 4.1. The total luminosity of the disk is greater for the perturbed disk (for a 20% increase in temperature for $r \leq 400R_g$) than the unperturbed disk as we would expect, since the wavelength-specific luminosity over the disk depends on the blackbody function $B_\lambda(T)$, which is greater for greater temperatures. Specifically, L_{disk} is approximately 2 times greater for the perturbed disk than the unperturbed disk. The contributions to the luminosity from wavelengths shorter than the Lyman-Limit also increases but is approximately 2.4 times greater for the perturbed disk demonstrating that the inner hotter regions of the disk are most responsible for emitting the shorter wavelengths of light in the spectrum of an AGN.

Presentation of Findings

This section presents two graphs and a table of values representing the impact on the spectrum after varying the temperature scale through the disk.

Figure 4.2 shows how the wavelength specific luminosity contribution functions are affected from perturbing the disk by increasing the temperature by 20% from the ISCO to $r = 400\ R_g$. The graph shows how within $r = 400\ R_g$, the wavelength specific luminosity contributions increase with the perturbation for all wavelengths and then drop back to the contribution functions shown in Figure 3.1 beyond $r = 400\ R_g$.

Figure 4.3 shows the spectrum of the perturbed and unperturbed disks. It can be seen that at longer wavelengths, the two spectra agree; however, at shorter wavelengths, the two spectra begin to deviate. By perturbing the disk, we simulated an increase in the dissipation locally in the disk, which increased the temperature, the flux and total power in the disk. The increase in temperature through the inner region of the disk (ISCO to $r = 400\ R_g$) mainly affects shorter wavelengths which are emitted from inner regions of AGN accretion disks. Consequently, we observe that the perturbed spectrum is increased in brightness and peaks at shorter wavelengths.

Table 4.2 gives the values in λL_λ at particular wavelengths depicted in Figure 4.2. The values in this table show that the model affects shorter wavelengths more than the longer wavelengths recorded. Specifically, the fractional difference noted in the table between the perturbed and unperturbed values in λL_λ, highlights that for $\lambda = 91.20$nm, there is a 90% increase in the spectral value, but only a 40% increase for $\lambda = 546.39$nm, and 20% increase for $\lambda = 912.0$nm. This is because they contribute primarily to the inner region of the disk where the temperature is affected by the model. It can also be seen that where the longer wavelengths contribute most lies close to or outside of positions in the disk greater than $r = 400\ R_g$ boundary imposed by the model. It is therefore expected that they will be impacted the least. Additionally, our observation that the spectra are impacted the most at short wavelengths explains why we observe AGN to become bluer as they become brighter, and redder as they become dimmer.

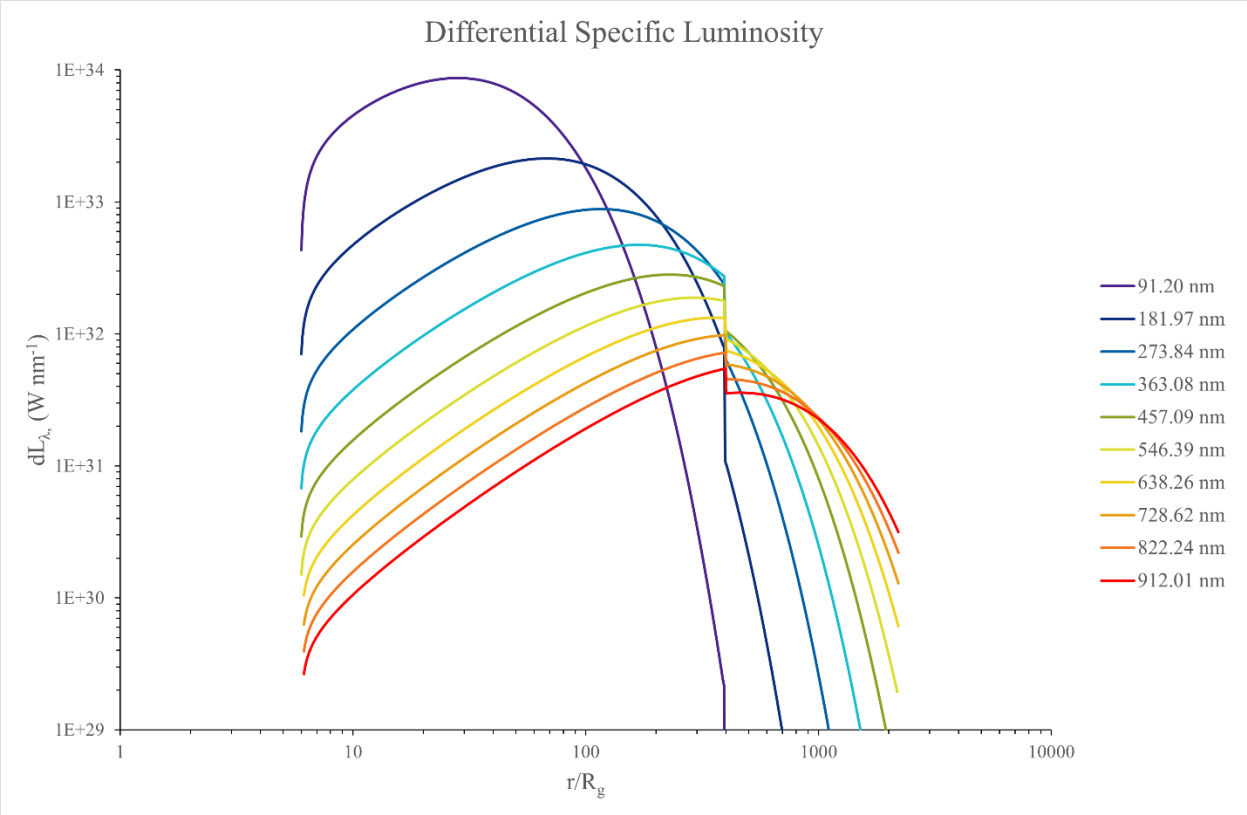

Figure 4.2 – A graph of the wavelength specific luminosity contributions over the disk for each of the ten wavelengths selected based off the Lyman-Limit for hydrogen. The graph is plotted for the input parameters for Model A and only shows the perturbed disk result from applying a 20% increase in the temperature at every point in the disk from the ISCO to $r = 400\ R_g$, at which point the temperature was returned to its original scale.

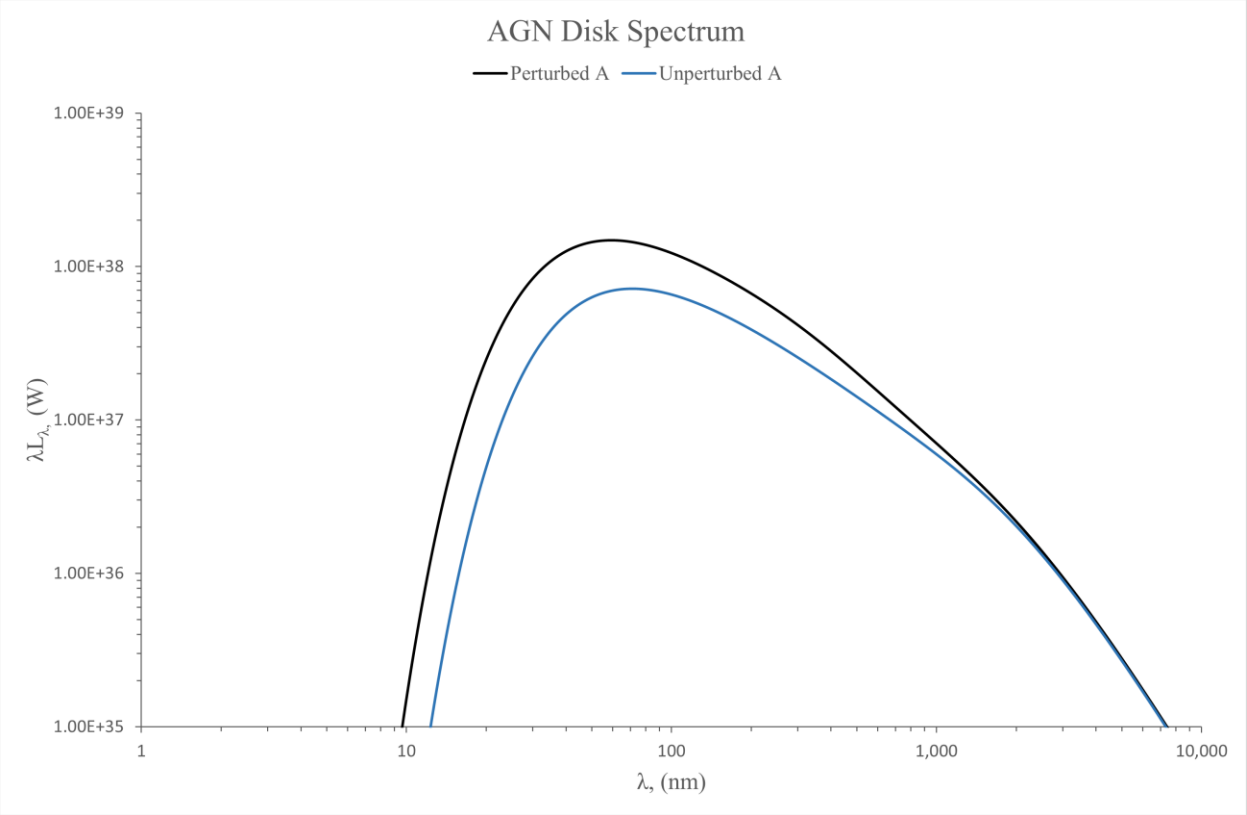

Figure 4.3 – A graph of the luminosity vs. wavelength producing the spectrum of the perturbed and unperturbed disks. The graph shows how the two spectra deviate at shorter wavelengths due to the increase in temperature by the model, and that the spectra agree at longer wavelengths.

	Model A		
λ (nm)	**Perturbed λL_λ (10^{38} W)**	**Unperturbed λL_λ (10^{38} W)**	**Fractional Difference of Unperturbed and Perturbed λL_λ**
91.20	1.2980	0.68230	0.902
181.97	0.73659	0.42427	0.736
273.84	0.46620	0.28155	0.656
363.08	0.32262	0.20598	0.566
457.09	0.23216	0.15768	0.472
546.39	0.17780	0.12745	0.395
638.26	0.14034	0.10552	0.330
728.62	0.11460	0.089594	0.279
822.24	0.095229	0.076957	0.237
912.01	0.081226	0.067368	0.215

Table 4.2 – A table of values in λL_λ at particular wavelengths for the perturbed and unperturbed AGN disk spectra appearing in Figure 4.2. The models are color coded to match Table 4.1 and Figure 4.2.

5. Final Conclusions

The first section of this paper discussed the structure of an accretion disk and its critical features, including temperature, radiative flux, and luminosity. We discussed that as matter is accreted onto the accretion disk, and viscous forces transport the matter further into the potential well, the loss in gravitational potential energy is converted into thermal energy and radiated away, creating the immense luminous power we observe from AGNs. We also discuss the Eddington Luminosity for our model to give the limiting bounds for which the accretion mode, structure, radiative properties, and the structure of accretion remain similar to our standard model.

Our results show that the inner region of an accretion disk is the hottest and emits the greatest share of the disks luminous power. An accretion disk with a fixed mass accretion rate around a more massive SMBH is cooler than for a disk around a less massive one and is more luminous for greater accretion rates. Specifically, the luminosity at each annulus of radius r in the disk depends on that radius's effective temperature scaled to the fourth power. The disk's local temperature depends on two parameters, the mass of the SMBH and the mass accretion rate. The temperature scales to the fourth root of the mass accretion rate M_{dot}, which is why for a fixed mass of the SMBH, a greater mass accretion rate results in a hotter and more luminous disk. The temperature also scales inversely to the square root of the mass, so for a fixed mass accretion rate a more massive SMBH has a cooler yet equally luminous accretion disk.

The second section of this paper discussed the emitted spectrum of an accretion disk, observing the dependence and contributions of selected wavelengths on the total luminosity and spectrum of the disk. The results show that the accretion disk spectra of AGN peak at ultraviolet (UV) wavelengths and for a fixed disk mass accretion rate, the accretion disks around less massive black holes are hotter and therefore have spectra that peak at shorter UV wavelengths and vice versa for spectra of accretion disks around more massive black holes. The shorter wavelengths in the observed spectrum are largely confined to arise and peak within inner regions of the disk where the temperature is hotter, whereas longer wavelengths are emitted from a broader range in the disk and peak in the outer disk where the temperature is cooler.

Finally, the characteristic variability of AGN accretion disks was discussed, and a simple temperature scale model was applied to the spectrum of the disks. Our results and model were

based on the proposal that a hot corona produces magnetic fields which fluctuate in the disk, causing local temperature fluctuations. As our model increased the temperature of the inner region of the disk from the ISCO to r = 400 R_g by 20%, the total luminous power of the accretion disk doubled approximately, with the luminous power contributions from wavelengths shortward of 91.20 nm increasing approximately by a factor of 2.4. This demonstrates that the shortest wavelengths contributing to the total luminosity of an accretion disk changed in their emission the most, as these wavelengths arise most prominently from the inner disk where our disk's temperature was perturbed, and the wavelengths which have significant contributions to the spectrum outside of r = 400 R_g fluctuated less.

6. References

Shields, G. (1999). A Brief History of Active Galactic Nuclei. *Astronomical Society of the Pacific, 111*(760), 661–678. https://www.jstor.org/stable/10.1086/316378

Carroll, B. W., & Ostlie, D. A. (2018). *An introduction to modern astrophysics* (Second edition). Cambridge University Press.

Shakura, N. I., & Sunyaev, R. A. (1973). Black holes in binary systems: Observational appearances. *Symposium - International Astronomical Union, 55*, 155–164. https://doi.org/10.1017/S007418090010035X

Hille, K. (2013, November 22). *Nasa's hubble gets the best image of bright quasar 3c 273* [Text]. NASA. http://www.nasa.gov/content/goddard/nasas-hubble-gets-the-best-image-of-bright-quasar-3c-273

Supermassive black hole at the heart of NGC 5548. (n.d.). Retrieved 27 April 2023, from https://www.esa.int/ESA_Multimedia/Images/2014/06/Supermassive_black_hole_at_the_heart_of_NGC_5548

Chandra: Resources: Quasars & agns(Illustrations). (n.d.). Retrieved 27 April 2023, from https://www.chandra.harvard.edu/resources/illustrations/quasar.html

Garner, R. (2017, October 6). *Messier 87* [Text]. NASA. http://www.nasa.gov/feature/goddard/2017/messier-87

Chandra: Educational materials: Stellar evolution: Stellar evolution—Cycles of formation and destruction. (n.d.). Retrieved 15 April 2023, from https://chandra.harvard.edu/edu/formal/stellar_ev/story/index8.html

Anderson, J., & Watzke, M. (2011, November 17). *Nasa - Cygnus X-1: A stellar mass black hole*. [Image Feature]. Retrieved 11 April 2023, from https://www.nasa.gov/mission_pages/chandra/multimedia/cygnusx1.html

Pereyra, N. A., Vanden Berk, D. E., Turnshek, D. A., Hillier, D. J., Wilhite, B. C., Kron, R. G., Schneider, D. P., & Brinkmann, J. (2006). Characteristic QSO Accretion Disk Temperatures from Spectroscopic Continuum Variability. *The Astrophysical Journal*, *642*(1), 87–95. https://iopscience.iop.org/article/10.1086/500919/pdf

Steady State Accretion Disk Model | introduction to astronomy | physics. (n.d.). MIT OpenCourseWare. Retrieved 10 April 2023, from https://ocw.mit.edu/courses/8-282j-introduction-to-astronomy-spring-2006/resources/shakurasunyaev/

Zdziarski, A., You, B., & Szanecki, M. (2022). Corrections to Estimated Accretion Disk Size due to Color Corrections, Disk Truncation, and Disk Wind. *The Astrophysical Journal Letters*, *939*(1). https://doi.org/10.3847/2041-8213/ac9474

Sun, M., Xue, Y., Brandt, W. N., Gu, W.-M., Trump, J. R., Cai, Z., He, Z., Lin, D., Liu, T., & Wang, J. (2020). Corona-heated accretion-disk reprocessing: A physical model to decipher the melody of agn uv/optical twinkling. *The Astrophysical Journal*, *891*(2), 178. https://doi.org/10.3847/1538-4357/ab789e

7. Appendix

Name	Symbol	Value	Unit
Solar Mass	$M_\odot$	1.98841×10^{30}	kg
Solar Luminosity	$L_\odot$	3.8419×10^{26}	W
Astronomical Unit	AU	$1.49597870700\times10^{11}$	m
Julian Light Year	ly	9.460730472×10^{15}	m
Julian Year	yr	3.1557600×10^{7}	s
Gravitational Constant	G	6.67430×10^{-11}	$N\ m^2\ kg^{-2}$
Speed of Light in a Vacuum	c	2.99792458×10^{8}	$m\ s^{-1}$
Stefan-Boltzmann Constant	σ_{SB}	5.670374419×10^{-8}	$W\ m^{-2}\ K^{-4}$
Boltzmann Constant	k	1.160451812×10^{4}	$K\ eV^{-1}$
Planck's Constant	h	6.62607015×10^{-34}	J s
Permittivity of Free Space	ε_0	$8.8541878128\times10^{-12}$	$F\ m^{-1}$
Electron Mass	m_e	$9.1093837015\times10^{-31}$	kg
Hydrogen Mass	m_H	$1.673532838\times10^{-27}$	kg

Table 7.1 – A list of physical and astronomical constants

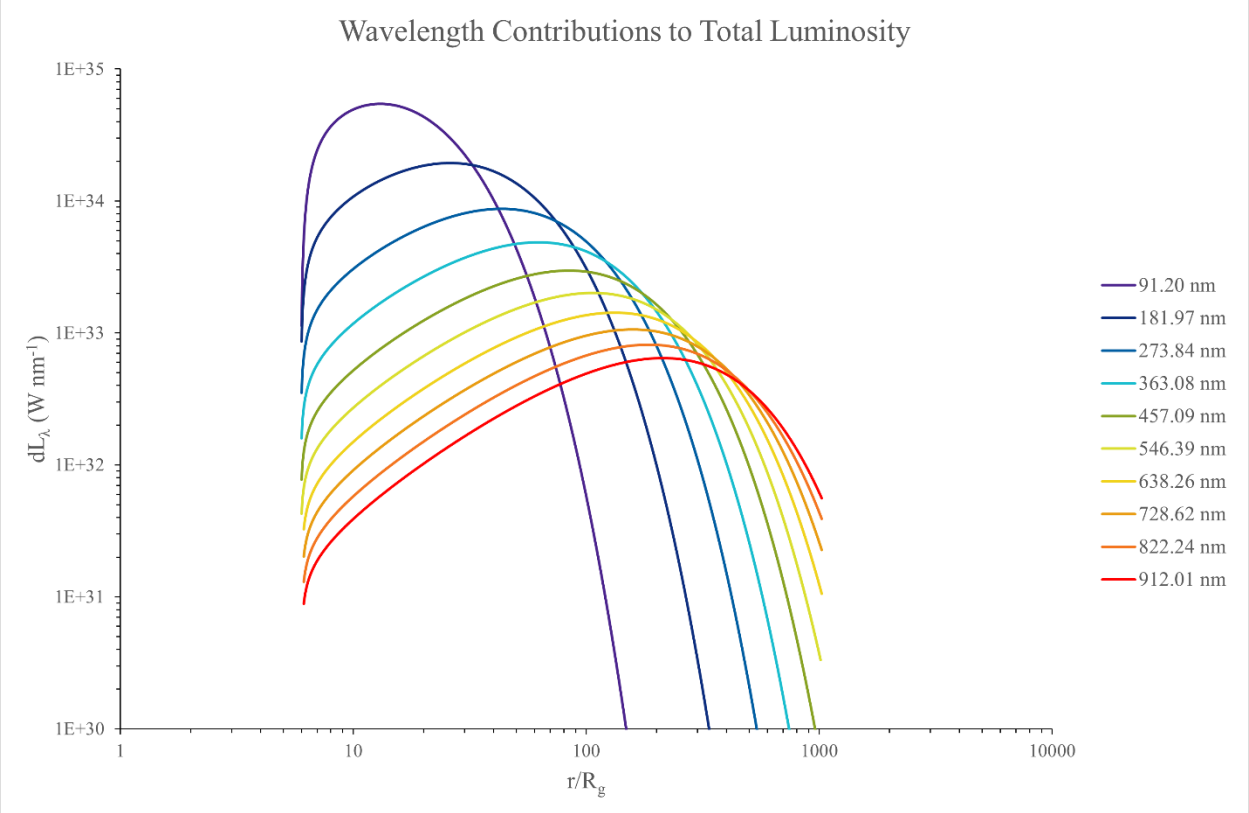

Figure 7.1 – A graph of differential wavelength specific luminosity vs. r/R_g for Model B.

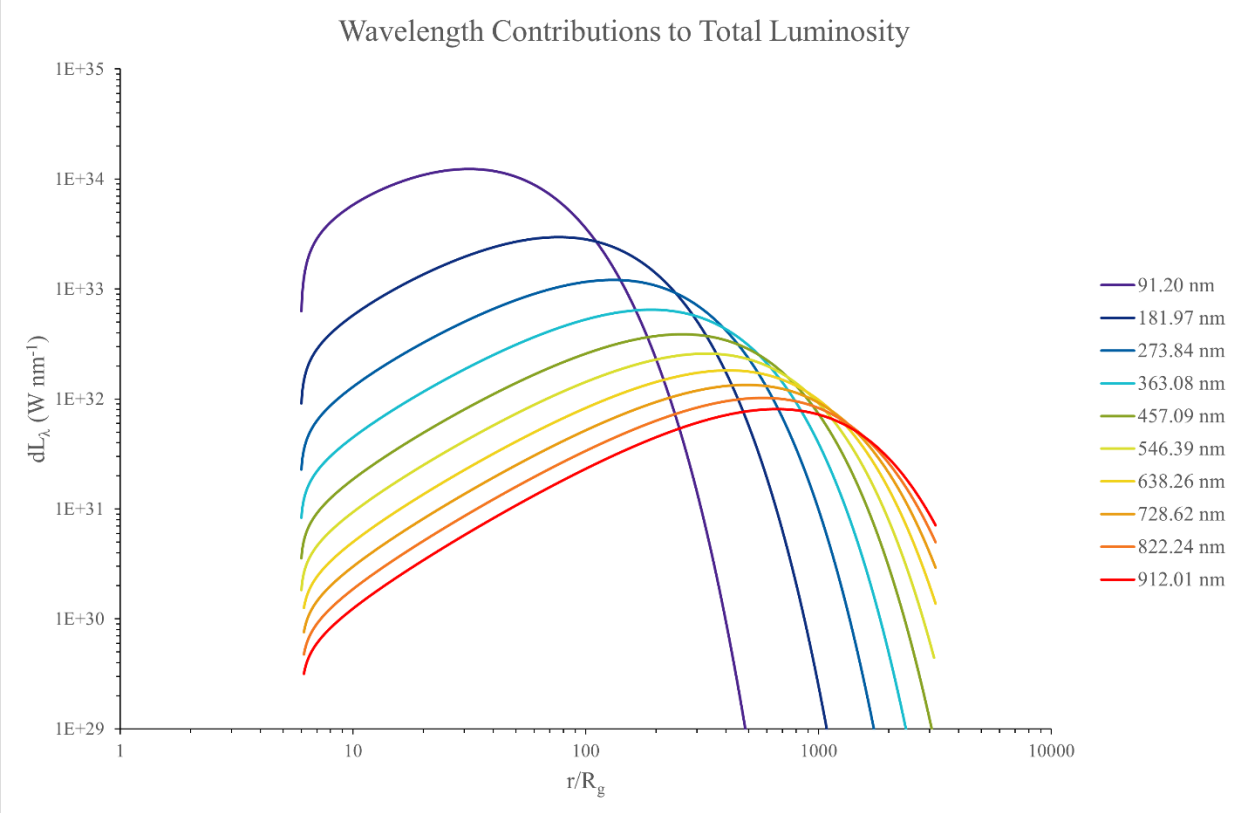

Figure 7.2 – A graph of differential wavelength specific luminosity vs. r/R_g for Model C.

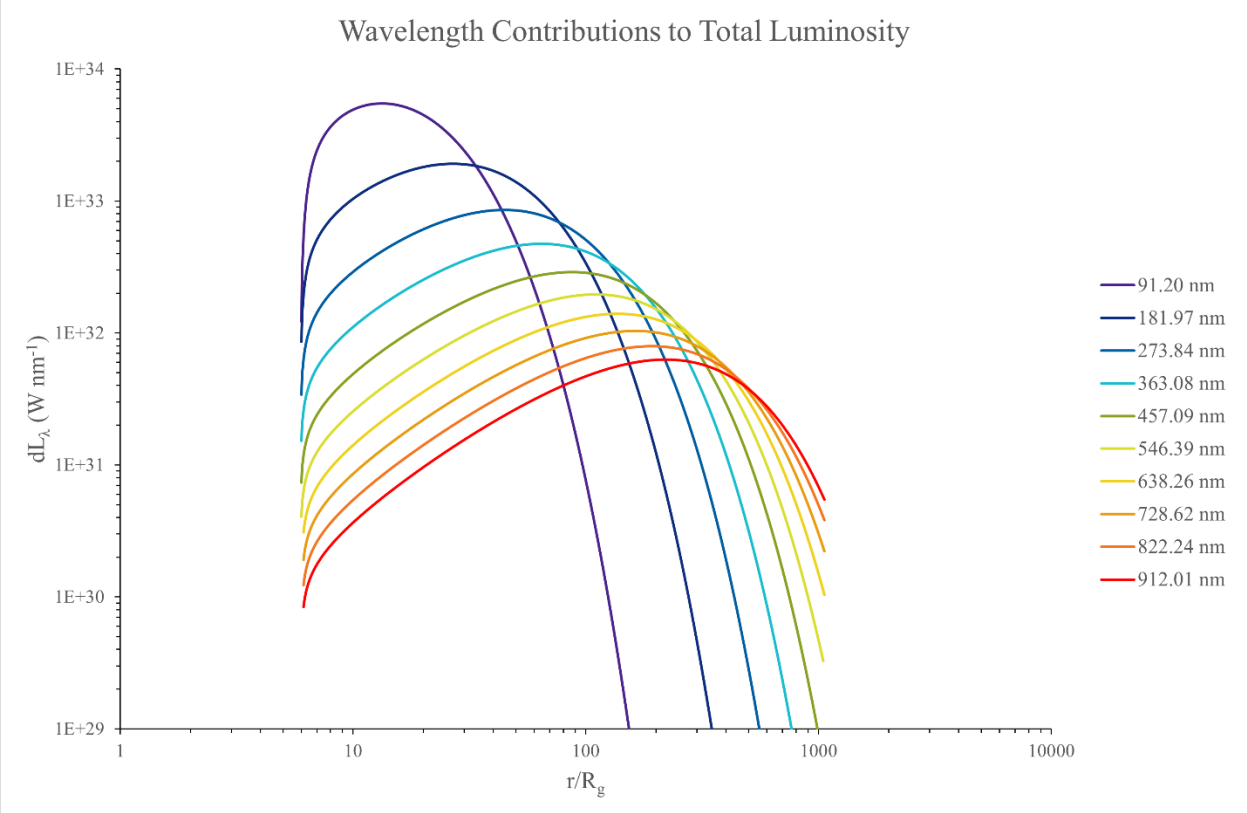

Figure 7.3 – A graph of differential wavelength specific luminosity vs. r/R_g for Model D.